Linköping Studies in Science and Technology,
Dissertation No. 1003

Near-infrared photodetectors based on Si/SiGe nanostructures

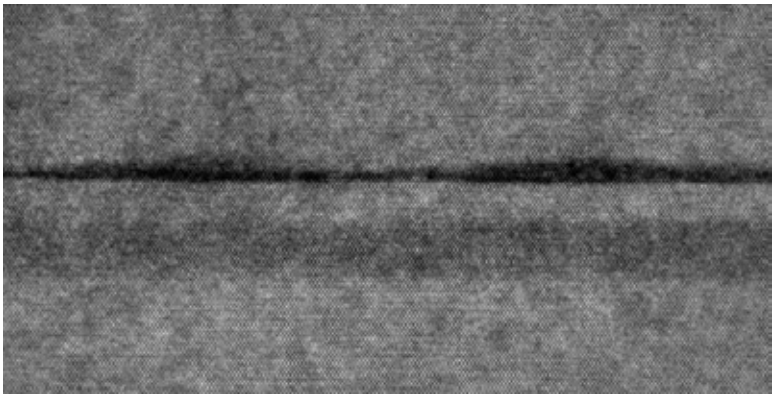

Surface and Semiconductor Physics
Department of Physics, Chemistry and Biology
Linköping University, S-581 83 Linköping, Sweden

Linköping 2006

Cover: HRTEM image of a **SiGe (QW)/Ge (QD)** photodetector structure.

ISBN: 91-85497-24-X
ISSN: 0345-7524

Printed in Sweden by LiU-Tryck, Linköping 2006

Abstract

Two types of photodetectors containing Ge/Si quantum dots have been fabricated based on materials grown by molecular beam epitaxy and characterized with several experimental techniques. The aim was to study new device architectures with the implementation of Ge nanostructures, in order to obtain high detection efficiency in the near-infrared range at room temperature.

Heterojunction bipolar phototransistors were fabricated with 10 Ge dot layers in the base-collector (b-c) junction. With the illumination of near-infrared radiation at 1.31 to 1.55 μm, the incident light would excite the carriers. The applied field across the b-c junction caused hole transport into the base, leading to a reduced potential barrier between the emitter-base (e-b) junction. Subsequently, this resulted in enhanced injection of electrons across the base into the collector, i.e., forming an amplified photo-induced current. We have therefore obtained significantly enhanced photo-response for the Ge-dot based phototransistors, compared to corresponding quantum dot p-i-n photodiodes. Responsivity values up to 470 mA/W were measured at 1.31 μm using waveguide geometry, and ~2.5 A/W at 850 nm, while the dark current was as low as 0.01 mA/cm^2 at –2 V.

Metal-oxide field-effect phototransistors were also studied. These lateral detectors were processed with three terminals for source, drain and gate contacts. The Ge quantum dot layers were sandwiched between pseudomorphically grown SiGe quantum wells. The detector devices were processed using a multi-finger comb structure with an isolated gate contact on top of each finger and patterned metal contacts on the side edges for source and drain. It was found that the photo-responsivity was increased by a factor of more than 20 when a proper gate bias was applied. With V_G above threshold, the measured response was 350 and >30 mA/W at 1.31 and 1.55 μm, respectively.

Properties of Si/$Si_{1-x}Ge_x$ nanostructures were examined, in order to facilitate proper design of the above mentioned transistor types of photodetectors. The carrier recombination processes were characterized by photoluminescence measurements, and the results revealed a gradual change from spatially indirect to direct transitions in type II $Si_{1-x}Ge_x$ islands with increased measurement temperature. Energy dispersive X-ray spectrometry of buried Ge islands produced at different temperatures indicated a gradual decrease of the Ge concentration with temperature, which was due to the enhanced intermixing of Si and Ge atoms. At a deposition temperature of 730°C the Ge concentration was as low as around 40%.

Finally, the thermal stability of the Si/SiGe(110) material system, which is a promising candidate for future CMOS technology due to its high carrier mobility, was investigated by high resolution X-ray diffraction reciprocal space mapping. Anisotropic strain relaxation was observed with maximum in-plane lattice mismatch in the [001] direction.

Preface

The objective of the thesis was to investigate Si/SiGe nanostructures for photodetector applications. The work involved material characterization and device layout optimization as well as electrical and optical analysis. The thesis is divided into two parts. The first part consists of an introduction to the research area and the field of Si/SiGe nanostructures together with descriptions of the experimental techniques used in the project. Some related unpublished data have also been included. The second part lists the publications included in the thesis.

Acknowledgements

First I would like to thank Prof. **Wei-Xin Ni**, my supervisor, for valuable assistance throughout this project. The guidance and the discussions have been invaluable for me, even though he has had new assignments on the other side of the world for the last one and a half year. I am very grateful to my co-supervisor, Prof. **Göran Hansson** for his active and constructive support. He has always had time for fruitful explanations and discussions. I would like to acknowledge Prof. **Per-Olof Holtz** for the cooperation, particularly within the field of photoluminescence. I thank the three above-mentioned persons for given me the opportunity to participate in the NANOPTO project.

Furthermore, I thank **Mats Larsson** for his collaboration and friendship during last several years. I also wish to thank my colleague and friend **Ming Zhao** for the collaboration and many laughs in the MBE lab. It has also been a pleasure to co-work with **Amir Karim**. Apart from interesting discussions and friendship, he has been very helpful in the TEM lab. I would also like to acknowledge **Adnane Bouchaib** for his cooperation in the process lab and Ivy Razado, my officemate, for putting up with me. I am very grateful to **Karl-Olof Brolin** for his outstanding technical support, **Kerstin Vestin** for the administrative work, and the other persons that I have worked with. My friends at IFM, especially Timo, Johan and Axel, I appreciate for their valuable discussions during lunch breaks and unforgettable memories from the golf course, and Naureen for her great kindness and friendship. I am also very thankful to my girlfriend, Auayporn "Pon" Jiemchooroj, for the fantastic support and memories of being together for the past year. Finally, I wish to express my gratitude to my parents for their support and believe in me.

Included papers

I. **SiGe (Ge-dot) heterojunction phototransistors for efficient light detection at 1.3-1.55 µm**

A. Elfving, G.V. Hansson, and W.-X. Ni, *Physica E* ***16****, 528 (2003).*

II. **Efficient near infrared Si/Ge quantum dot photodetector based on a heterojunction bipolar transistor**

A. Elfving, M. Larsson, P.-O. Holtz, G.V. Hansson, and W.-X. Ni, *Material Research Society Symposium Proceedings* ***770,*** *I.2.2 (2003).*

III. **Infrared photodetectors based on a Ge-dot/SiGe-well field effect transistor structure**

A. Elfving, G. V. Hansson, W.-X. Ni, *Electrochemical Society Proceedings, SiGe: Materials, Processing, and Devices,* ***7****, 1053 (2004).*

IV. **A three-terminal Ge dot/SiGe quantum well MOSFET photodetector for near infrared light detection**

A. Elfving, A. Karim, G. V. Hansson, and W.-X. Ni, *in manuscript.*

V. **Spatially direct and indirect transitions observed for Si/Ge quantum dots**

M. Larsson, A. Elfving, P. O. Holtz, G. V. Hansson, and W.-X Ni, *Appl. Phys. Lett.* ***82****, 4785 (2003).*

VI. **Band alignment studies in Si/Ge quantum dots based on optical and structural investigations**

M. Larsson, A. Elfving, W.-X. Ni, G. V. Hansson, and P. O. Holtz, *submitted to Phys. Rev. B.*

VII. **Thermal stability of SiGe/Si(110) investigated by high-resolution X-ray diffraction reciprocal space mapping**

A. Elfving, M. Zhao, G. V. Hansson, and W.-X. Ni, *in manuscript.*

Contributions not included in the thesis

Gate Controlled Ge/SiGe QD/QW Photo-MESFETS for High Photoresponse at 1.31-1.55 μm

A. Elfving, G. V. Hansson, and W.-X. Ni, *Proceeding of the 1st IEEE international conference on group-IV photonics, Hongkong, Sept. 28 – Oct. 1, 2004.*

Ge-QD/SiGe-QW Superlattice for Near Infrared Photodetectors

A. Elfving, G. V. Hansson, W.-X. Ni, *Proceedings of the symposium on Si-based photonics: towards true monolithic integration, E-MRS, Strasbourg, May 24-28, 2004.*

Efficient near infrared Si/Ge quantum dot photo-detector based on a heterojunction bipolar transistor

A. Elfving, M. Larsson, P.-O. Holtz, G.V. Hansson, and W.-X. Ni, *Invited talk at the MRS Spring Meeting, San Francisco, April 21-24, 2003.*

Compositional analysis of Si/SiGe quantum dots using STEM and EDX

A. Karim, A. Elfving, M. Larsson, W.-X. Ni, and G. V. Hansson, *to be published in Proceedings of the SPIE - The International Society for Optical Engineering, **6129** (2006).*

Si-Photonic Devices for Integrated Optoelectronics

W.-X. Ni, and A. Elfving, *"Silicon Heterostructure Handbook" edited by John Cressler, Taylor & Francis, Boca Raton, 2006, ch. 7.4, pp. 751.*

Origin of abnormal temperature dependence of electroluminescence from Er/O-doped Si diodes

G. V. Hansson, W.-X. Ni, C.-X. Du, A. Elfving, and F. Duteil, *Appl. Phys. Lett. **78**, 2104 (2001).*

Reversed quantum-confined Stark effect and an asymmetric band alignment observed for type II Si/Ge quantum dots

M. Larsson, P. O. Holtz, A. Elfving, G. V. Hansson, and W.-X. Ni, *Phys. Rev. B **71**, 113301 (2005).*

Surface diffusion limited nucleation of Ge dots on the Si(001) surface

Y.-H. Wu, C.-Y. Wang, A. Elfving, G. V. Hansson, and W.-X. Ni, *Materials Science and Engineering B **89**, 151 (2002).*

Si-based photonic transistor devices for integrated optoelectronics

W.-X. Ni, A. Elfving, M. Larsson, G.V. Hansson, and P.-O. Holtz, *Invited talk at the 3rd International Conference on SiGe Epitaxy and Heterostructures, Santa Fe, March 2003.*

1.54 μm light emitting devices based on Er/O-doped Si layered structures grown by molecular beam epitaxy

W.-X. Ni, C.-X. Du, F. Duteil, A. Elfving, and G. V. Hansson, *Optical Materials **17**, 65 (2001).*

Luminescence study of Si/Ge quantum dots

M. Larsson, A. Elfving, P. O. Holtz, G. V. Hansson, and W.-X. Ni, *Physica E **16**, 476 (2003).*

SiGe/Si:Er light emitting transistors

W.-X. Ni, C.-X. Du, G. V. Hansson, A. Elfving, A. Vörckel, and Y. Fu, *Proceeding of the NATO workshop: Towards the First Silicon Laser, 429 (2003).*

Si-based photonic transistor devices for integrated optoelectronics

W.-X. Ni, A. Elfving, M. Larsson, G.V. Hansson, and P.-O. Holtz, *Proceedings of the 3rd international conference on SiGe(C) epitaxy and heterostructures, 251 (2003).*

Photoluminescence study of Si/Ge quantum dots

M. Larsson, A. Elfving, P. O. Holtz, G. V. Hansson, and W.-X. Ni, *Surface Science **532-535C**, 832 (2003).*

Mid/Far–Infrared Detection using a MESFET with Modulation Doped Ge-dot/SiGe-Well Multiple Stacks in the Channel Region

B. Adnane, M. Zhao, A. Elfving, B. Magnusson, and W.-X. Ni, *Proceeding of the 1st IEEE international conference on group-IV photonics, Hongkong, Sept. 28 – Oct. 1, 2004.*

Low-temperature Molecular Beam Epitaxy Growth of Si/SiGe THz Quantum Cascade Structures on Virtual Substrates

M. Zhao, A. Elfving, B. Adnane, W.-X. Ni, P. Townsend, S.A. Lynch, D.J. Paul, C. C. Hsu, and M. N. Chang, *Proceedings of the 4th International Conference on Si Epitaxy and Heterostructure, 118 (2005).*

Asymmetric band alignment at Si/Ge quantum dots studied by luminescence from p-i-n and n-i-p structures

M. Larsson, A. Elfving, P.-O. Holtz, G. V. Hansson, and W.-X. Ni, *Proceedings of the 27th International Conference on the Physics of Semiconductors, ICPS 2004, Flagstaff, Arizona.*

Contents

Abstract

Preface

Acknowledgements

Included papers

Contributions not included in the thesis

1. Introduction 1

2. The Si/SiGe material system 5

2.1 Fundamental physics of Si/SiGe 5

2.2 Heterostructures and low dimensional Si/SiGe strauctures 14

2.3 Photonic applications of Si/SiGe nanostructures 17

3. Growth and experimental characterization of Si/SiGe nanostructures 21

3.1 Molecular beam epitaxy 21

3.2 X-ray diffraction 25

3.3 Atomic force microscopy 28

3.4 Transmission electron microscopy 29

3.5 Photoluminescence 31

3.6 Detector device fabrication 31

3.7 Photoconductivity measurements 34

4. Si/SiGe photodetectors 37

4.1 General description of a semiconductor photoconductor 37

4.2 Ge/Si quantum dot photodetectors 40

5. Fundamental study of Si/SiGe nanostructures 47

5.1 Size, shape and density of Ge islands 47

5.2 Composition in $Si_{1-x}Ge_x$ islands 50

5.3 Vertical alignment of Ge islands 52

5.4 Si/SiGe(110) 53

6. Ge dot phototransistors 57

6.1 Heterojunction bipolar phototransistor 57

6.2 Lateral phototransistor 62

7. Summary of included papers. 69

7.1 Paper I 69

7.2 Paper II 70

7.3 Paper III 71

7.4 Paper IV 71

7.5 Paper V 72

7.6 Paper VI 72

7.7 Paper VII 73

Chapter 1

Introduction

When Jöns Jacob Berzelius, who spent his adolescence in Linköping, first successfully isolated elemental silicon (Si) in 1823, he probably never realized how important this material would be. After almost two centuries, Si has nowadays been known as the most important semiconductor material because of the chip technology, which gives a large impact to the development of human civilization, society and daily life. About 50 years after Berzelius discovery, the Russian scientist Dmitri Mendeleev predicted another silicon-like material that he called eka-silicon. This material was not discovered until 1886, when the German chemist Clemens Winkler could isolate the material from a mineral. He named the material germanium (Ge) as an honor for his country.

Si and Ge have been established in the semiconductor technology for several decades since the first Ge transistor was invented in December 1947 [1,2]. The fact that Si dominates more than 95 % of the present semiconductor market, even though III-V semiconductors show superior high-speed performance, has several reasons. i) The low material cost and one of the natural elementary resources with the largest quantity on earth. *ii*) The insulators of Si, such as SiO_2 and Si_3N_4, have far better properties than other semiconductor insulators, and the processes to fabricate these are much more well-established. *iii*) A less complex fabrication scheme of Si has implied extremely large fabrication yields and, hence, very cost effective. *iv*) Si has a more than three times higher thermal conductivity than GaAs, which reduces the requirement of external cooling. This is needed because of the larger number of devices in a

chip and the increased clock frequency, which raises the power consumption and requires efficient heat dissipation.

Si and Ge are semiconductors belonging to group-IV in the periodic table. The electronic structure of Si and Ge is similar and each atom has four near neighbors covalently bonded in a tetragonal configuration. As a result, Si and Ge can be alloyed forming $Si_{1-x}Ge_x$ with unique properties. High-quality heterostructures, where multi-layers of strained Si/SiGe layers altering each other, have been successfully produced by the accurately controlled epitaxial growth techniques, which provide single crystalline material with very low densities of defects.

Device scaling has so far basically followed the prediction made by Gordon Moore, the so-called Moore´s law. At present, the 65-nm Si-CMOS technology has been commercialized for production, while over a billion of devices can be integrated into one chip. Furthermore, in the laboratories, many devices are already fabricated in nanometer size, which implies that the fundamental knowledge of quantum mechanics is an important issue for future nano-sized device technology.

The development of nanoelectronics therefore demands the implementation of new materials that should be Si-compatible but with enhanced electric and photonic properties for further device scaling. Si/Ge has thus been considered as a useful and promising material for this purpose. New methods for improving the transport properties in Si/SiGe by increasing the material strain have been widely studied. Process- and mechanically-induced strain has also been demonstrated and commercialized [3,4]. A good example of strain-induced carrier mobility enhancement is the new CMOS components that have been implemented in Intels 90 nm logic nanotechnology [5].

In photonics, on the other hand, Si and Ge suffer from their poor optical properties and cannot compete with the direct band gap semiconductors. Si/SiGe nanostructures nowadays offer new solutions for improving the optical efficiency of the materials. Although there is still a lack of commercially valuable Si-based active photonic devices, efficient light sources and detectors based on Si/SiGe would be a breakthrough that will open possibilities for the new system-on-a-chip to incorporate photonic devices with Si nanoelectronics. Moreover, the requirement of emitters and photodetectors in optical interconnects have recently been highlighted by the International Technology Roadmap for Semiconductors (ITRS), which proposed that the bandwidth of electrical interconnects will limit the circuit performance of CMOS ICs in the near future [6]. While the optical clock distribution may be operated from an external source, the importance of integrated light detectors in the receiver system has been

suggested. Si-based infrared photodetectors are probably the most attractive candidate for this purpose due to the possibility of integration into the logic IC chips.

It is therefore of high interest to use strain engineering to tailor the material properties for the requested purposes. For example, nano-sized self-assembled Ge islands, so-called quantum dots, in which quantum confinement effects occur in all three directions, is a useful material for light absorption. Except for the enhanced absorption probability, the long carrier lifetime can enhance the detection efficiency further.

The project work presented in this thesis has thus been motivated by such a demand. The objectives for the studies are to establish knowledge and competence to engineer and produce Si/Ge layered and low-dimensional heterostructures for the desired properties, in combination with innovative design of device structures to study and fabricate some efficient detector devices that can be useful for the above-mentioned purposes.

References

[1] J. Bardeen and W. H. Brattain, Phys. Rev. series II **74**, 230 (1949)

[2] J. Bardeen and W. H. Brattain, Phys. Rev. series II, **75**, 1208 (1949)

[3] J. L. Hoyt, Electrochemical Society Proceedings, SiGe: Materials, Processing, and Devices, **7**, 15 (2004)

[4] B. M. Haugerud, L. A. Bosworth, and R. E. Belford J. Appl. Phys. **94**, 4102 (2003).

[5] T. Ghani, M. Armstrong, C. Auth, M. D. Giles, K. Mistry, A. Murthy, L. Shifren, S. Thompson, and M. Bohr, Electrochemical Society Proceedings, SiGe: Materials, Processing, and Devices, **7**, 681 (2004).

[6] International Technology Roadmap of Semiconductors (2004), http://www.itrs.net/Common/2004Update/2004 00 Overview.pdf

Chapter 2

The Si/SiGe material system

2.1 Fundamental physics of Si/SiGe

Si has a diamond crystal structure, which can be considered as two face-centered cubic Bravais lattices displaced by one quarter of the body diagonal. In Fig. 2.1, the diamond structure is illustrated together with the corresponding first Brillouin zone with high-symmetry points indicated. The lattice constant of Si is a_{Si} = 5.431 Å and the band gap is E_{gSi} = 1.12 eV at 300 K [1]. As shown in Fig. 2.2, Si is an indirect band gap material with the highest valence band in the center of the Brillouin zone (Γ-point), and the lowest conduction band in the Δ-point at $\mathbf{k} \approx 0.85 \times 2\pi/a$ towards the X-point. The Δ-valleys are six-fold degenerate due to the lattice symmetry.

The valence band of Si around the Γ-point is more complicated due to the asymmetric band structure. Degenerate heavy-hole (hh) and light-hole (lh) bands constitute the valence band maximum together with a split-off band separated by the split-off energy (0.044 eV). As a result, holes are generally distributed in both the hh- and lh-bands very close to the Brillouin zone center ($k \approx 0$).

Like Si, Ge has the diamond lattice structure with a_{Ge} = 5.658 Å [1]. It is an indirect band gap material (E_{gGe} = 0.66 eV at room temperature) with a four fold degenerated conduction band edge in the L-point. However, the unstrained $Si_{1-x}Ge_x$ alloy has a Si-like

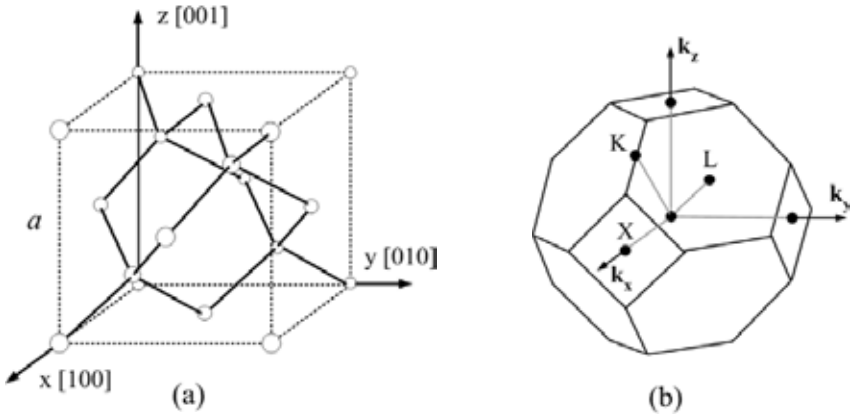

Figure 2.1. The diamond crystal structure of Si (a), and the corresponding first Brillouin zone with a few high-symmetry points (b).

energy band structure with a band gap close to E_{gSi} (with the lowest conduction band near the X-point) for x < 0.85, which is shown in Fig. 2.3. For Ge concentrations above 0.85, the SiGe material has a Ge-like band structure and the band gap is strongly dependent on *x*.

2.1.1 Strain in Si/SiGe

The lattice constant of $Si_{1-x}Ge_x$ is dependent on the composition, and with a first order approximation it can be described by Vegard´s law

$$a_{SiGe} = (1-x)a_{Si} + xa_{Ge} \tag{2.1}$$

where *x* is the fraction of Ge ($0 < x < 1$). Due to the difference in lattice constant, lateral and vertical strain is introduced in a $Si_{1-x}Ge_x$ layer, pseudomorphically grown on a Si substrate. In

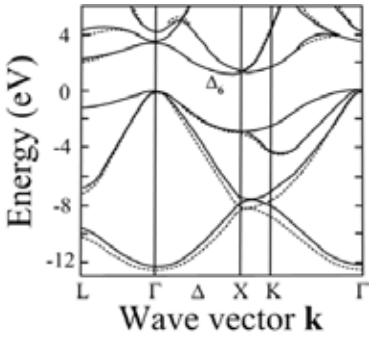

Figure 2.2. The Si energy bands in different directions, calculated using nonlocal pseudo-potentials (solid lines) and local pseudo-potentials (dashed lines) [2].

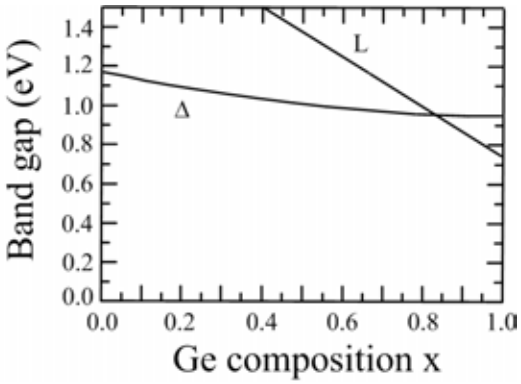

Figure 2.3. The band gap dependence of unstrained $Si_{1-x}Ge_x$ as a function of Ge concentration, *x*. Up to $x \approx 0.85$, the material has a Si-like band structure with the lowest conduction band edge in the Δ-valley. Above $x \approx 0.85$ the conduction band is Ge-like and the band gap is strongly dependent on *x* [3].

general, the in-plane lattice constant of the strained layer follows that of the substrate. The Poisson effect requires that the material almost conserves its volume, implying that tetragonal distortion is introduced perpendicular to the surface as well. The strain (ε) and lattice mismatch (*f*) are defined as

$$\varepsilon_{//} = \frac{a_{//}^{L} - a^{L}}{a^{L}} = \frac{a_{//}^{L}}{a^{L}} - 1 \tag{2.2a}$$

$$\varepsilon_{\perp} = \frac{a_{\perp}^{L} - a^{L}}{a^{L}} = \frac{a_{\perp}^{L}}{a^{L}} - 1 \tag{2.2b}$$

$$f_{//} = \frac{a_{//}^{L} - a_{//}^{S}}{a_{//}^{S}} = \frac{a_{//}^{L}}{a_{//}^{S}} - 1 \tag{2.3a}$$

$$f_{\perp} = \frac{a_{\perp}^{L} - a_{\perp}^{S}}{a_{/\perp}^{S}} = \frac{a_{\perp}^{L}}{a_{\perp}^{S}} - 1 \tag{2.3b}$$

where S and L are indices representing the substrate and layer, respectively, and a^L is the lattice constant of unstrained epi-layer material.

Based on the bulk elastic theory for homogeneous deformation, Hornstra and Bartels proposed a relationship between the lattice mismatch and the material elastic constants, *c* [4]. By applying a stress to the material so that $\varepsilon = \varepsilon_{//}$ in all directions and thereafter removing the normal strain component by an amount $-(\varepsilon_{//} - \varepsilon_{\perp})$, coherent epitaxy was modeled. The ratio $\varepsilon_{//}/(\varepsilon_{//} - \varepsilon_{\perp})$ was derived to be

$$\{100\}: \qquad \frac{\varepsilon_{//}}{\varepsilon_{//} - \varepsilon_{\perp}} = \frac{c_{11}}{c_{11} + 2c_{12}} = \frac{1-\nu}{1+\nu} \tag{2.4a}$$

$$\{110\}: \qquad \frac{\varepsilon_{//}}{\varepsilon_{//} - \varepsilon_{\perp}} = \frac{c_{11} + \frac{1}{2}C}{c_{11} + 2c_{12}} \tag{2.4b}$$

$$\{111\}: \qquad \frac{\varepsilon_{//}}{\varepsilon_{//} - \varepsilon_{\perp}} = \frac{c_{11} + \frac{2}{3}C}{c_{11} + 2c_{12}} \tag{2.4c}$$

where $\nu = c_{12}/(c_{12} + c_{11})$ is the Poisson ratio and $C = 2c_{44} - c_{11} + c_{12}$ is a correction factor. The elastic constants for Si and Ge are given in table 2.1.

Table 2.1. Poisson ratios and elastic constants in 10^{10} Pa for Si and Ge. The values are taken from ref. 4.

	c_{11}	c_{12}	c_{44}	C	ν
Si	16.58	6.39	7.96	5.73	0.278
Ge	12.85	4.83	6.68	5.34	0.273

In the case of partial strain relaxation, $\varepsilon_{//}$ and $(\varepsilon_{//} - \varepsilon_{\perp})$ should be reduced by $f_{//}$, given in Eq. 2.3a. Consequently, the average (or equivalent) lattice mismatch for a layer can be written as

$$\text{Generally:} \qquad f = \frac{a^L}{a^S} - 1 = (f_{\perp} - f_{//})\frac{\varepsilon_{//}}{\varepsilon_{//} - \varepsilon_{\perp}} + f_{//} \tag{2.5a}$$

$$\text{For } \{100\}: \qquad f = \frac{a^L}{a^S} - 1 = (f_{\perp} - f_{//})\frac{1-\nu}{1+\nu} + f_{//} \tag{2.5b}$$

2.1.2 Strain relaxation in Si/SiGe

The elastic energy stored in the epi-layer is proportional to the square of the strain and it also increases linearly with the layer thickness. When the epi-layer thickness is above a critical value, it relaxes by the formation and propagation of misfit dislocations. Hence, the strain in the material is released. The propagation of typical misfit dislocations normally occurs by glide on {111} planes inclined to the surface [5]. According to Peierls barrier model, the energy of a dislocation is proportional to the square of its Burgers vector, **b**. (The relationship between the Burgers vector and the dislocation line direction defines the character of the dislocation, i.e. edge or screw dislocations, etc.) The lowest energy corresponds to the shortest lattice translation Burgers vector laying in the {111} planes, which is $a/2\langle 110\rangle$ for the SiGe cubic diamond lattice.

Dislocations with edge character, which are the most common in relaxed materials, have always a corresponding Burgers vector perpendicular to the dislocation line direction. Therefore the edge dislocations are following the in-plane $\langle 011\rangle$ directions in the orthogonal intersections formed by the {111} planes. Consequently, SiGe(100) relaxes symmetrically in all directions. Fig. 2.4 shows the surface roughness of a relaxed $Si_{0.8}Ge_{0.2}$(100) layer. The surface reveals a typical cross-hatch pattern parallel to the $\langle 011\rangle$ directions, which is a result of the dislocation lines aligned along this group of orientations.

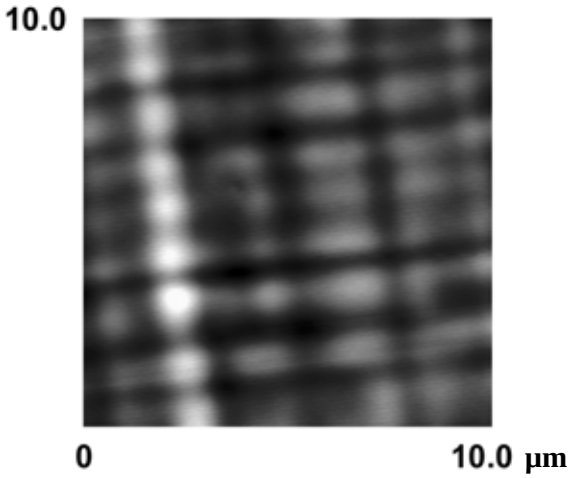

Figure 2.4. Atomic force microscopy image of a relaxed SiGe layer on a Si(100) substrate. The typical cross-hatch pattern in the [110] directions is revealed [6].

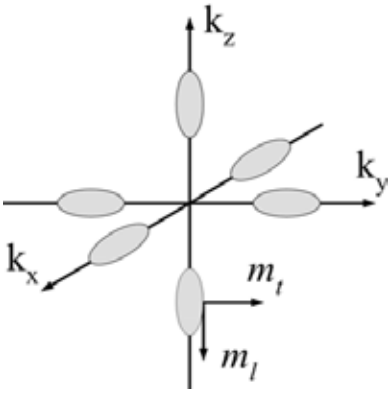

Figure 2.5. Constant energy surfaces for electrons around the Δ-valley in Si. The electron effective mass varies with the direction of transport, which is indicated in the figure.

The formation of dislocations via strain relaxation reduces the electrical and optical quality of the material, and it limits the growth parameters for the lattice-mismatched Si/Ge system. The process is also thermally activated if the SiGe layer is metastable. This has to be considered during high temperature device processing steps and operation.

2.1.3 Transport properties

Fig. 2.5 illustrates constant energy surfaces of electrons in unstrained Si. The energy dispersion is not symmetric around the valleys, which explains the elongated energy surfaces. The relation between effective mass and energy dispersion results in different transverse and longitudinal effective electron masses, denoted by m_t and m_l, respectively. For Si, the values of the transverse and longitudinal effective masses are $m_t = 0.19m_o$ and $m_l = 0.92m_o$, where m_o is the electron rest mass [1]. The carrier mobility is associated with the effective mass via

$$\mu = \frac{e\tau}{m^*} \tag{2.6}$$

where e is the electron charge and τ is the mean free time governed by all scattering processes. By applying an electric field, for example parallel to the [001] direction, the electrons are accelerated in the negative z-direction. Electrons occupying the Δ-valleys on the k_z-axis have low mobility because of the relatively large mass value. On the other hand, electrons located in the energy valleys on the k_x- and k_y-axes have smaller effective mass

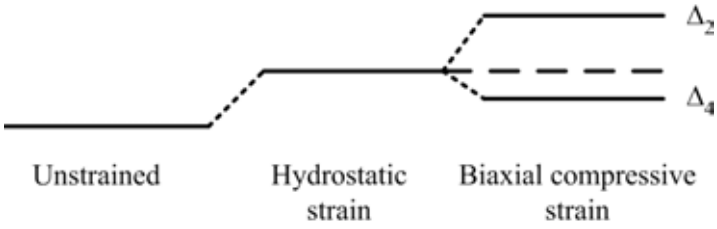

Figure 2.6. The energy shift of the Δ-bands under hydrostatic strain and biaxial compressive strain.

values, and thus higher mobility. Accordingly, 2/3 of the accelerated electrons have high mobility when an electric field is applied along one of the principal axes. However, at higher fields, so-called intervalley scattering can reduce the mobility. In this case, an electron is scattered from a high to a low mobility valley, involving one or several phonons in order to conserve the crystal momentum. High carrier mobility is of importance in most types of semiconductor devices to achieve high-speed/high-frequency ICs.

One way to improve the carrier mobility is to engineer the energy band structure of the Si/SiGe material system by manipulation of strain conditions using e.g. advanced thin film growth techniques. The interaction between atoms in the crystal will change by varying the distance between them. As a result, degenerate bands will shift or split under applied stress. Due to the Si-like band structure for most SiGe alloys, it is most relevant to consider the Δ-point under different strain conditions, which is schematically pictured in Fig. 2.6. As mentioned above, all six bands are degenerated when no strain field is applied. Under hydrostatic strain, i.e. stress is applied in all directions of the crystal, the atoms become closer to each other. From the tight binding model, this causes a shift of the lowest conduction band edge towards higher energies. If uni- or biaxial strain is applied to the material, the degenerate bands split into two levels due to the broken symmetry.

In the case of pseudomorphic growth of SiGe on Si, the SiGe layer is biaxially compressively strained in the x-y plane (in plane), while it is uniaxially strained along the z-direction (normal to the surface) that is of tensile character. The broken symmetry in the crystal structure leads to a downshift of the Δ_4-valleys in the x-y plane, while the Δ_2-valleys along the z-axis lifts to higher energies [7]. Neglecting the effect of hydrostatic stress, the average energy of the six bands remains the same after applying the stress. Thus, the shift of the Δ_2-valleys is larger than for the Δ_4-valleys. The constant energy surface diagram in Fig 2.7a illustrates the effects of the band splitting. Most of the electrons are now occupying the

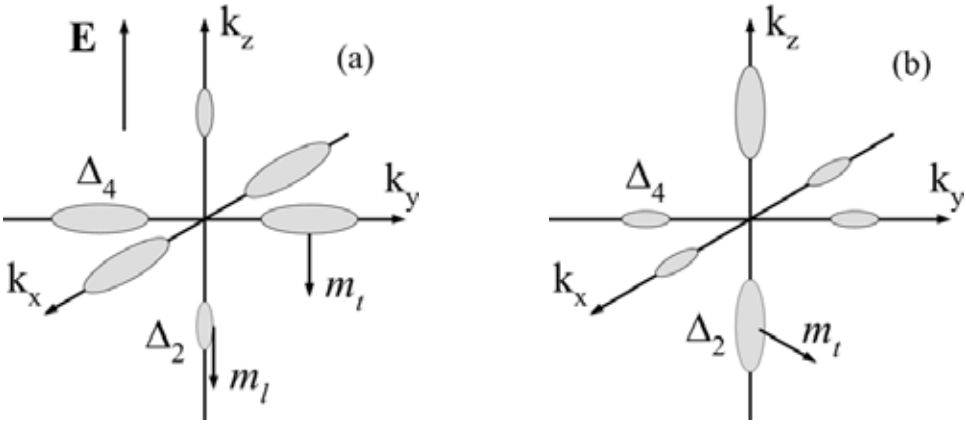

Figure 2.7. Constant energy surfaces for the electrons when the material is compressively strained in two directions (a), and when the material is biaxially tensilely strained (b).

larger low-energy valleys (larger "pockets" in the figure). Consequently, when an E-field along the z-axis is applied, the average electron mobility is higher due to the fact that a majority of the electrons now have a lower effective mass. This is not the only effect that causes an increased mobility. Intervalley scattering can only occur if the sum of the electron and phonon energies is larger than the valley separation. Since the band splitting has increased the energy gap between Δ_4 and Δ_2-valleys, there is less probability for this scattering event to happen.

The splitting of the valence band in biaxially strained SiGe is very complex. Generally, the lh band shifts to lower energies (for holes), causing band mixing or so-called hybridization. The lowest energy band has an hh character far from the Γ-point and a lh-like shape with more strongly bended band curvature close to the Brillouin zone center. Fig. 2.8 shows calculated valence bands near to the Γ-point in $[\bar{1}10]$ and [110] directions when compressive biaxial stress is applied [8,9]. The dashed curves illustrate the bands in unstrained material. Repopulation of holes into the light hole valley at the Γ-point together with a reduction of the intervalley scattering increase the hole mobility, similar to the case of electrons. The common MOSFET configuration has its channel along the [110] direction. For that reason, strained SiGe on Si(100) is more suitable in the channel of p-MOS, since one can not make use of the gain in electron mobility in the [110] directions.

In n-MOS with a [110]-channel, the highest electron mobility is obtained under biaxial tensile strain. Oppositely to the previous case, the Δ_2-valleys become the lowest energy bands containing most of the electrons. From Fig. 2.7b, it is obvious that there is a large gain in

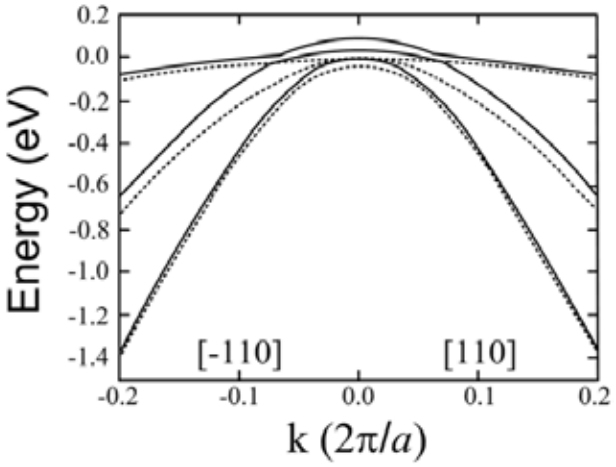

Figure 2.8. Valence bands along the [110] directions when 1 GPa biaxial stress is applied to the material (solid lines). The valence bands were calculated using the non-local empirical pseudo-potential method. The dashed curves indicate the bands under no strain. From [8] after [9].

mobility when the E-field is applied along [110]. In fact, acceleration of electrons in any direction in the x-y plane is very efficient due to their low transverse effective mass. Si grown pseudomorphically on a relaxed SiGe substrate (a so-called virtual substrate) is one example of fabrication of biaxial tensile material [10].

2.1.4 Optical properties

Si and Ge are poor materials for optical emission due to their indirect band gaps. The **k**-conservation rule requires involvement of one or several phonons in optical transitions. This makes any transition inefficient and slow. Accordingly, luminescence spectra for pure Si or Ge only reveal phonon replicas. For the same reason, absorption processes are far less efficient than those of direct band gap materials. However, when incident photon energies are larger than the band gap energy at the Γ-point, absorption can occur without phonons since the transition is direct in **k**-space.

In SiGe alloys, the lattice symmetry is broken when short-range potentials perturbate the well-ordered lattice of a perfect crystal, which thereby relaxes the momentum conservation rule and enhances the optical properties. Mixing of states with different **k**-values also permits no-phonon transitions [11]. Luminescence spectra of SiGe structures are therefore characterized not only by phonon replicas, but also a contribution from no-phonon emission.

Intersubband transitions in doped Si/SiGe structures are also of importance for many applications. The absence of strong polar optical phonon scattering at long wavelengths ($\lambda > 5$

μm) keeps the long carrier lifetime constant up to 100 K [12,13]. Unlike III-V materials, this allows for high temperature operation of SiGe light emitters in the mid- and far infrared regions.

2.2 Heterostructures and low dimensional Si/SiGe structures

In order to improve the optical properties of the Si/SiGe material, much research efforts have been focused on fabrication and characterization of nano-sized SiGe structures. Epitaxial growth with an atomic level precision of layer-control has permitted the formation of Si/SiGe heterojunctions with very sharp interfaces and abrupt conduction and valence band potential variations. Figs. 2.9a and b show the band edge energies as a function of Ge concentration for strained $Si_{1-x}Ge_x$ on Si, and strained Si on $Si_{1-x}Ge_x$, respectively, calculated from the model solid theory [3,14]. One can see that both strained SiGe and Si keep a Si-like band structure throughout the entire Ge composition range up to $x = 1$, which differs from the bulk SiGe alloys. The strain effects on the Si and SiGe band structures were also confirmed by non-local empirical pseudo-potential calculations by Rieger et. al. [9]. Fig. 2.9c, schematically shows an example of the potential band alignment when first $Si_{1-x}Ge_x$ and then pure Si is pseudomorphically grown on $Si_{1-y}Ge_y$ for $x > y$. In fact, the band offset is not only a result of the different band gaps of Si and SiGe, more importantly, the strain effects give a large contribution to the band offset [15]. In heterostructures of Si/SiGe, where the two materials are sandwiched, discontinuities in the energy bands can act as potential barriers for carriers. The electrical and optical properties are further modified when the layer thickness is reduced to nanometer size. Dimensions comparable with the de Broglie wavelength of the carriers cause quantum mechanical carrier confinement.

2.2.1 Properties of low dimensional structures

A very thin layer with a small band gap sandwiched between two semiconductors with larger band gaps is called a quantum well (QW). The carriers are then localized in the thin layer and quantum mechanical effects have to be considered, i.e. discrete energy levels form for the confined carriers along the layer stacking direction, while restricting the carrier motion to

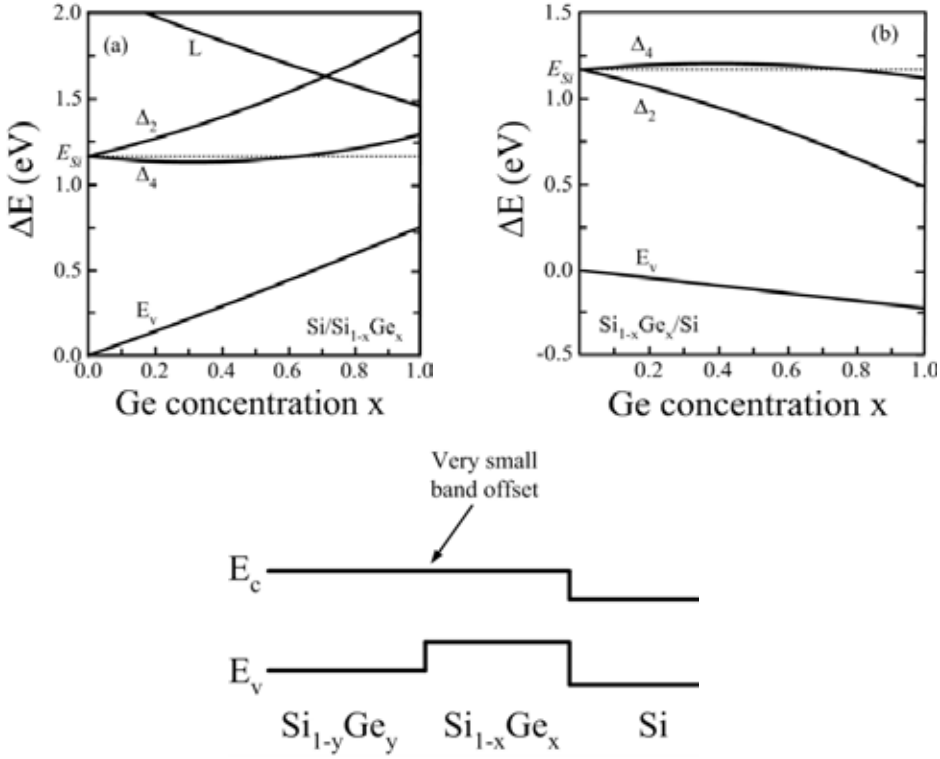

Figure 2.9. The x dependence of the energy bands for strained $Si_{1-x}Ge_x$ grown on Si (a), as well as for strained Si grown on $Si_{1-x}Ge_x$ (b) [12]. An example of the band alignment when strained $Si_{1-x}Ge_x$ and Si is grown on $Si_{1-y}Ge_y$ when x > y (c).

only the other two dimensions. Furthermore, if the low band gap material is fabricated as a stripe, the above-mentioned carrier quantum confinement occurs in two directions. This structure is called a quantum wire (QWR), meaning that the carrier motion is only allowed along the wire direction. When a small band gap material is surrounded in all directions by a large band gap material, it is called a zero-dimensional quantum dot (QD). The carriers are then confined in all three directions.

Several properties of low dimensional structures are explained by the density of states (DOS), which gives the number of states per unit volume and energy. In the case of a bulk semiconductor, the DOS function has a square-root dependence on energy. Confining the carriers in one or several directions changes the DOS, ending up with a completely discrete spectrum for QDs. Furthermore, the energy states can be tailored by varying the size of the quantum structures. The energy position of the quantum states shifts due to the fact that the energy is approximately inversely proportional to the width in x-, y-, or z-directions. This

means that transitions between the discrete electronic states in a large QD are somewhat red-shifted compared to the corresponding transitions levels in a small QD.

Carrier confinement in low dimensional Si/SiGe heterostructures is of largest importance for the optical properties. The previously mentioned relaxation of the crystal momentum conservation, due to Si-Ge alloying, is further enhanced when the structure dimensions are reduced. Carrier confined in real space will have a wave function that is spread out in **k**-space. This implies that the overlap of the electron and hole wave functions becomes larger and the probability for no-phonon transitions is increased.

2.2.2 Stranski-Krastanov growth of Ge/Si islands

The Ge quantum dots in the samples of this thesis have been produced by the so-called Stranski-Krastanov growth mode. This is illustrated in Fig. 2.10, where the atomic planes are represented as lines in the figure. The process is only applicable when the epi-layer has a lattice mismatch with the substrate. As stated above, biaxial compressive strain is introduced in Ge when it is grown on a Si substrate. As long as the layer is thin enough, the growth remains two-dimensional. However, when the layer thickness exceeds a critical value (typically a few mono-layers), the accumulated strain in the material is so high that the epi-layer rapidly relaxes elastically in order to reduce its total energy. As a result, three-dimensional islands are formed and the growth changes essentially into a three-dimensional growth mode, with islands randomly distributed on the sample surface. The thin Ge layer prior to the formation of 3D islands is called wetting layer (WL). Due to the elastic lattice relaxation, the dislocation density is very low as long as the Ge deposition is limited [16]. Accordingly, introduction of dislocations are preceded by the formation of coherently strained Ge islands. For device applications, it is necessary to cap the dots with Si. From both theory and experiments, it is established that the dot relaxation leads to introduced strain in the Si above and below the islands [17-20]. According to Fig. 2.9a, the band alignment of a Ge island is of type II for $x \geq 0.8$, which means that excited holes and electrons are confined in the dots and the surrounding Si, respectively. In fact, type II band alignment is experimentally verified even at lower Ge concentrations due to the splitting of the Δ-band in the Si around the dots [21,22].

It has to be mentioned that Ge islands formed in the Stranski-Krastanov growth mode have a relatively large lateral diameter compared to the dot height. This leads to a larger degree of quantum carrier confinement in the growth direction. Therefore, it is in many cases reasonable to consider the Ge 3D island as a 2D nanostructure similar to the QW.

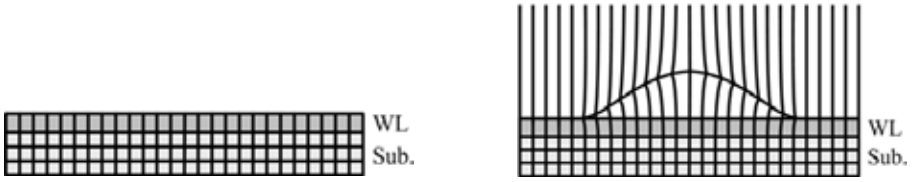

Figure 2.10. The principle of Stranski-Krastanov growth of Ge islands. First the growth is 2-dimensional (a), while the growth becomes 3-dimensional above the critical thickness. In (b) the island is shown after capping. Observe the strain in the capping layer just above the island apex (no vertical planes are shown in the cap).

2.3 Photonic applications of Si/SiGe nanostructures

It is of greatest interest to fabricate commercial optical devices based on Si/SiGe due to the ability to integrate optoelectronics with Si nanoelectronics. Moreover, the band gap of SiGe is suitable for applications in the near-infrared range where optical fibers have their transmission windows. Another application field in the future could be the implementation of Si/SiGe emitters and detectors in optical interconnects, which is proposed to replace the now existing electrical interconnects [23]. Nevertheless, optoelectronic components have so far been much more challenging due to the above mentioned poor optical properties of Si and SiGe. In the case of Ge QD photonic devices, other problems occur, such as variations in the island size distribution and composition during growth.

As a first step, it would be a great success if SiGe/Si QW or Ge/Si QD light emitting diodes (LEDs) could be fabricated with a high efficiency. p-i-n photodiodes have been produced in research laboratories, which show island related luminescence peaks in the near infrared range under forward bias conditions [24-27]. However, the efficiency is still too low for these LEDs to be commercialized to reach the market. The reverse process, i.e. absorption processes, in low dimensional Si/SiGe have also been intensively studied with the objective to fabricate Si-based photodetectors [28,29]

In the long perspective, a major goal has been to develop a Si-based laser. The incorporation of nano-sized Ge islands would not only be preferable with respect to the important wavelength range. A temperature independent threshold, which is lower compared to conventional bulk semiconductor lasers, is expected [30,31].

The lack of efficient light sources in the mid- and far infrared spectral regions have increased the interest for Si/SiGe THz cascade emitters during the last few years. These

structures are based on strain symmetrized SiGe/Si superlattices grown on SiGe virtual substrates. Since the SiGe layers have higher Ge fraction than the virtual substrate, holes are confined in the SiGe layers and surrounded with Si barriers. The emission relies on optical inter-subband transitions that are expected to be either within the SiGe QWs or via tunnelling through the Si barrier into the adjacent QW [6,32,33]. With an applied bias, multiple recombinations will amplify the output intensity if the number of superlattice periods is large. It is proposed that the SiGe THz cascade laser can be realized in the future, which would be useful for medical imaging and pollution monitoring etc.

References

[1] K. W. Böer, *Survey of Semiconductor Physics*, 2nd edition, vol. 1, John Wiley & Sons Inc., New York (2002).

[2] J. R. Chelikowsky and M. L. Cohen, Phys Rev. B **14**, 556 (1976).

[3] C. G. Van de Walle, and R. M. Martin, Phys. Rev. B **34**, 5621 (1986).

[4] J. Hornstra, and W. J. Bartels, J. Cryst. Growth, **44**, 513 (1978).

[5] J.P. Hirth and J. Lothe, Theory of Dislocations, McGraw-Hill, New York (1968).

[6] M. Zhao, W.-X. Ni, P. Townsend, S. A. Lynch, D. J. Paul, C. C. Hsu, and M. N. Chang, Thin Solid Films, in press.

[7] R. People, and J. C. Bean, Appl. Phys. Lett. **48**, 538 (1986).

[8] T. Ghani, M. Armstrong, C. Auth, M. D. Giles, K. Mistry, A. Murthy, L. Shifren, S. Thompson, and M. Bohr, Electrochemical Society Proceedings, SiGe: Materials, Processing, and Devices, **7**, 681 (2004).

[9] M. M. Rieger, and P. Vogl, Phys. Rev. B **48**, 14276 (1993).

[10] D. J. Paul, J. M. Ryan, P. V. Kelly, G. M. Crean, J. M. Fernandéz, M. Pepper, A. N. Broers, and B. A. Joyce, Solid State Electronics, **41**, 1509 (1997).

[11] M. V. Klein, M. D. Sturge, and E. Cohen, Phys. Rev. B **25**, 4331 (1982).

[12] P. Murzyn, C. R. Pidgeon, J.-P. R. Wells, I. V. Bradley, Z. Ikonic, R.W. Kelsall, P. Harrison, S. A. Lynch, D. J. Paul, D. D. Arnone, D. J. Robbins, D. Norris, and A. G. Cullis, Appl. Phys. Lett. **80**, 1456 (2002).

[13] B. N. Murdin, W. Heiss, C. J. G. M. Langerak, S.-C. Lee, I. Galbraith, G. Strasser, E. Gornik, M. Helm, C. R. Pidgeon, Phys. Rev. B **55**, 5171 (1997).

[14] C. G. Van de Walle, Phys. Rev. B **39**, 1871 (1989).

[15] W.- X. Ni and G. V. Hansson, Phys. Rev. B **42**, 3030 (1990).

[16] D. J. Eaglesham, and M. Cerullo, Phys. Rev. Lett. **64**, 1943 (1990).

[17] K. Brunner, Rep. Prog. Phys. **65**, 27 (2002).

[18] O.G. Schmidt, O. Kienzle, Y. Hao, K. Eberl, and F. Ernst, Appl. Plys. Lett. **74**, 1272 (1999).

[19] J. H. Seok and J. Y. Kim, Appl. Phys. Lett. **78**, 3124 (2001).

[20] M. Grundmann, O. Stier, and D. Bimberg, Phys. Rev. B **52**, 11969 (1995).

[21] M. Larsson, A. Elfving, P. O. Holtz, G. V. Hansson, and W.-X. Ni, Appl. Phys. Lett. 82, 4785 (2003).

[22] A. Karim, A. Elfving, M. Larsson, W.-X. Ni, and G. V. Hansson, to be published in Proceedings of the SPIE - The International Society for Optical Engineering, **6129** (2006).

[23] International Technology Roadmap of Semiconductors (2004), http://www.itrs.net/Common/2004Update/2004 00 Overview.pdf

[24] Q. Mi, X. Xiao, J. C. Sturm, L. C. Lenchyshyn, M. L. W. Thewalt, Appl. Phys. Lett, **60**, 3177 (1992).

[25] R. Apetz, L. Vescan, A. Hartmann, C. Dieker, and H. Luth, Appl. Phys Lett. **66**, 445 (1995).

[26] T. Brunhes, P. Boucaud, S. Sauvage, F. Aniel, J.-M. Lourtioz, C. Hernandez, Y. Campidelli, O. Kermarrec, D. Bensahel, G. Faini, and I. Sagnes, Appl. Phys. Lett. **77**, 1822 (2002).

[27] M. Stoffel, U. Denker, and O. G. Schmidt, Appl. Phys. Lett. **82**, 3236 (2003).

[28] T. P. Pearsall, Appl. Phys. Lett. **60**, 1712 (1992).

[29] L. Colace, A. DiVergillio, S. Vaidyanathan, T. P. Pearsall, H. Presting, and E. Kasper, Appl. Surf. Sci. **102**, 272 (1996).

[30] Y. Arakawa, and H. Sakaki, Appl. Phys Lett. **40**, 939 (1982).

[31] M. Asadsa, Y. Miyamoto, and Y. Suematsu, IEEE J. of Quantum Electronics **22**, 1915 (1986).

[32] D. J. Paul, S. A. Lynch, R. Bates, Z. Ikonic, R. W. Kelsall, P. Harrison, N. J. Norris, S. L. Liew, A. G. Cullis, D. D. Arnone, C. R. Pidgeon, P. Murzyn, J.-P. R. Wells, and I. V. Bradley, Physica E **16**, 147 (2003).

[33] R. Bates, S. A. Lynch, D. J. Paul, Z. Ikonic, R. W. Kelsall, P. Harrison, S. L. Liew, N. J. Norris, A. G. Cullis, W. R. Tribe, and D. D. Arnone, Appl. Phys. Lett. **83**, 4092 (2003).

Chapter 3

Growth and experimental characterization of Si/SiGe nanostructures

3.1 Molecular beam epitaxy

All samples presented in this work were produced by solid-source molecular beam epitaxy (MBE). This technique is based on evaporation of Si and Ge in an ultra-high vacuum (UHV) chamber. In order to achieve constant growth rates, well-defined melts are produced with electron-gun (e-gun) evaporators. The low pressure during operation allows Si and Ge atoms to reach the substrate without collisions. After condensation on the normally heated substrate surface, a crystalline film is formed. Depending on the substrate temperature, atomic fluxes and surface morphology, the deposited layer can be single-crystalline, poly-crystalline or amorphous. Assuming a Maxwellian velocity distribution, the number of atoms striking the surface per second and unit area can be approximately written as [1]

$$F = \frac{p}{\sqrt{2\pi m k_B T}} \tag{3.1}$$

where, F is the flux, p is the vapor pressure and m is the atomic mass. The growth can proceed in several different modes. Temperature, lattice strain effects and binding energy of the ad-atoms etc. determines which growth mode that will be dominant. In the case of 2-D growth,

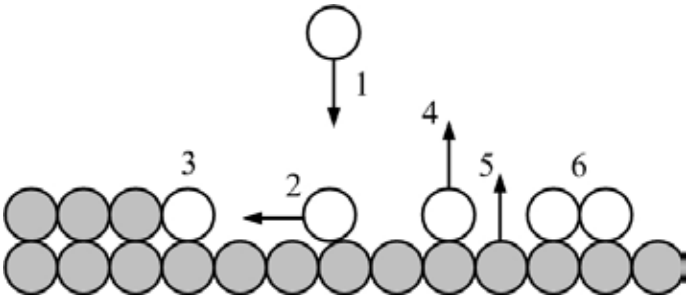

Figure 3.1. Examples of processes occurring at the surface during growth. 1. molecule arrival, 2. surface diffusion, 3. binding to a kink or step, 4. desorption, 5. surface segregation, 6. nucleation.

an ad-atom diffuses to an energetically favorable position at the surface where the surface energy is minimized, generally at an atomic step or a kink, which is shown in Fig. 3.1. In principle, the growth is therefore occurring laterally, layer-by-layer, but due to limited surface diffusion new atomic steps are normally formed during growth.

As shown in the figure, the ad-atoms can also undergo desorption, nucleation and segregation. Unlike chemical vapor deposition (CVD), no chemical reactions occur during the process leading to an almost constant growth rate with temperature. However, if the substrate temperature is high enough, a small deposition rate variation may occur because of the desorption process, which varies with the temperature. The desorption rate is associated with the so-called mean residence time, τ_a, given by [2]

$$\tau_a = \frac{1}{\nu_a} \exp\left[\frac{E_a}{k_B T}\right] \tag{3.2}$$

where ν_a is the atomic vibration frequency and E_a is the adsorption energy. At low temperatures, τ_a becomes large and more atoms have time bind to the surface while there is less time for the ad-atom to stay on the surface when the temperature increases. Nevertheless, τ_a is typically larger than 1 ms for Si growth, which gives a very high probability for a nucleation event to occur before desorption. As a result, desorption can be neglected in most cases, and its rate is varying between ~10^{-15} and ~10^{-2} ML/s from 450 to 950°C for Si on Si(100) growth [3]. This should be compared with typical Si deposition rates and growth temperatures, which are in most cases > 0.3 ML/s and < 800°C, respectively. Hence, the growth rate is not sensitive by temperature variations.

Doping is controlled independently by evaporation sources, so-called effusion cells. Typically B and Sb are used for p- and n-type doping. Segregation of dopant atoms to the surface has been a major problem for producing distinct doping profiles in Si epi-layer structures. Segregation is a thermally activated process, and the effect is also dependent on the growth rate. It is mainly due to two causes: *i)* atomic size differences between the dopants and the host matrix, and *ii)* binding energy differences between host-dopant bonds and host-host atom bonds as well as the energy of dangling bonds [4].

Sb have particularly been difficult to incorporate in the Si matrix. Several solutions to minimize the dopant surface segregation effect have been suggested, such as solid phase epitaxial (SPE) regrowth [5,6], or incorporation of doping atoms by the assistance of accelerated Si^+ ions towards a negatively biased substrate [7,8]. The most successful method solving the segregation problem during MBE growth is to ionize the dopant atoms and accelerate them towards the substrate with an external bias. In this case, the atoms have high enough kinetic energy to penetrate some distance into the layer, and it has been shown that the incorporation probability increases several orders of magnitude using this method, depending on the acceleration voltage and substrate temperature [9].

3.1.1 MBE equipment and growth procedure

During the thesis work, device-quality layered structures were grown in a Baltzer UMS 630 MBE system, dedicated for Si and Ge studies. It consists of one main chamber, one load-lock chamber, and one preparation chamber, where pre-annealing can be implemented. A schematic drawing of the MBE equipment is shown in Fig. 3.2. Excellent vacuum conditions in the chambers are achieved by turbo molecular pumps together with liquid nitrogen-cooled Ti sublimation pumps. The base pressure is $< 1\times10^{-10}$ mbar in the growth chamber before deposition. Even though most of the samples during the work were grown on 3 or 4-inch Si substrates, the system is designed for wafer sizes up to 5 inches, and the three chambers can totally load up to 12 wafers at the same time. The main chamber includes two Si and one Ge e-gun evaporators and three home-made resistively heated effusion cells for doping with B, Sb, and C, respectively. In addition, Sb dopant atoms are supplied by a low-energy ion source, which consists of an effusion cell with a discharge chamber for ionization, ion optics for extraction, and a unit for deflection and focusing of the ion beam [10]. The ion beam is deflected away from the neutral Sb flux by the optics as the source is mounted 11° from the direction of the substrate. Hence, deposition of neutral Sb atoms is minimized.

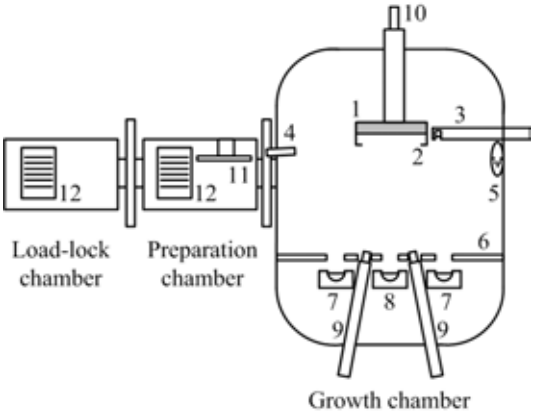

Figure 3.2. Schematic illustration of the Balzer UMS 630 MBE system, in which all structures included in this work have been grown. 1. graphite substrate heater, 2. sample holder, 3. mass-spectrometer, 4. e-gun for RHEED, 5. florescent RHEED screen, 6. water-cooled baffle, 7. e-beam evaporators for Si, 8. e-beam evaporator for Ge. 9. doping sources for B and Sb, 10. motor stage for sample rotation, 11. pre-heating unit, 12. sample magazines.

During growth, the beam fluxes of Si and Ge are monitored by a mass-spectrometer, which is connected by a feedback loop to the MBE control units and the e-guns. The automatic focus adjustment of the e-beam results in an extremely fast response, leading to a very stable deposition rate. The Sb^+ ion flux (current) is measured by a translatable Farady cup close to the substrate.

The Si(100) substrates experience the following cleaning steps before loaded into the chamber. *i)* Rinse in water, *ii)* dip in 2-5 % hydrofluoric acid (HF) to remove native SiO_2, *iii)* UV ozone exposure for at least 5 min, which removes carbon atoms from the surface ($2C + O_2 + h\nu \rightarrow 2CO$) and leaves a ~1 nm carbon-free SiO_2 on the surface, *iv*) dip in HF (2-5 %) to remove this oxide, and *v)* UV ozone exposure for one minute to achieve a thin protective oxide just before loading the substrates into the load-lock chamber. Prior to growth, the Si wafer is annealed *in situ* at ~825°C for about 8 min, which removes the thin oxide and gives a flat and atomically cleaned surface without contaminants. This process is monitored by reflection high-energy electron diffraction (RHEED) and after a few minutes at 825°C, a typical 2×1 reconstruction pattern is revealed for the Si(100) surface.

In most cases, the growth procedure begin with a high temperature Si buffer layer, normally at 700°C, to ensure a high quality growth surface. Thereafter, a somewhat thinner low temperature buffer layer is deposited at the same temperature as the active structure. The active region is normally deposited at a growth rate of typically 0.4-1 Å/s and 0.1-0.25 Å/s for Si and Ge, respectively.

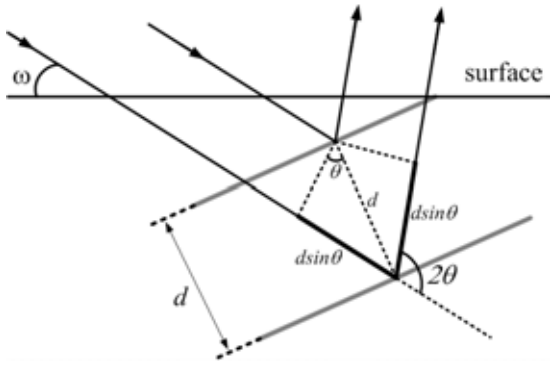

Figure 3.3. X-rays diffracted on a family of atomic planes. The Bragg condition is satisfied when the path difference is an integer number of the wavelength.

3.2 X-ray diffraction

A non-destructive and highly sensitive technique to characterize strain, composition and relaxation in crystals is X-ray diffraction (XRD). X-rays elastically scattered from the crystal interfere constructively following Bragg´s law

$$2d \sin\theta = m\lambda \tag{3.3}$$

where d is the distance between lattice planes, m is the order (integer), λ is the wavelength and θ is the angle between the incident X-rays and the planes, from where the X-rays are scattered. Hence, the more commonly defined angle 2θ is the angle between incoming and diffracted X-ray beams. Bragg´s law reveals that the path difference must be equal to an integer times the wavelength, as shown in Fig. 3.3.

In a reciprocal space representation, the Ewald sphere construction is visualizing the Bragg conditions. Here, a row of reciprocal lattice points represents lattice planes separated by a distance d in real space. The reciprocal lattice points are separated $2\pi/d$ along the direction normal to the lattice planes, each point with distance $2\pi m/d$ from the origin. The radius of the Ewald sphere is equal to the wave vector of the incident X-rays, $|\mathbf{K}| = 2\pi/\lambda$, which is drawn in such a way that it ends at the origin, as illustrated in Fig. 3.4. The diffracted beam with wave vector $\mathbf{K'}$, is determined from $\mathbf{K'} = \mathbf{K} + \mathbf{G}$, where $\mathbf{G}$ is the scattering vector, which is normal to the set of planes involved in the scattering event. The diffraction condition is satisfied only if there is a reciprocal lattice point on the Ewald sphere surface at $\mathbf{G}$. Using

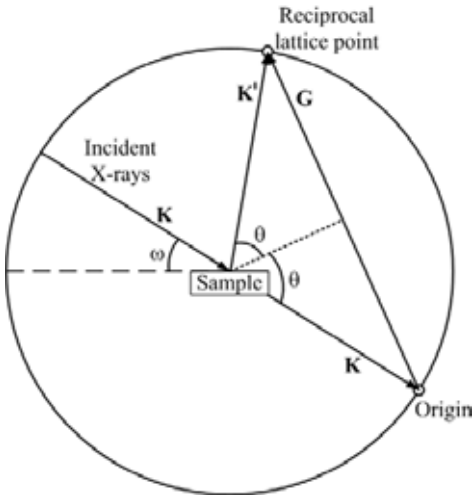

Figure 3.4. The Ewald sphere construction for a Bragg reflection in reciprocal space.

the fact that $|\mathbf{G}| = 2\pi m/d$, $|\mathbf{K}| = |\mathbf{K}'|$ for an elastic scattering event, together with the geometry from Fig. 3.4, it can be shown that Bragg´s law follows from the reciprocal space representation

$$\frac{|\mathbf{G}|}{2} = \frac{\pi m}{d} = |\mathbf{K}'|\sin\theta = \frac{2\pi}{\lambda}\sin\theta \Rightarrow 2d\sin\theta = m\lambda \qquad (3.4)$$

In the present work, XRD measurements were carried out using a Philips X'pert high-resolution X-ray diffractometer, using an asymmetric triple-axis analyzer and a hybrid four-crystal Ge(220) monochromator in front of a Cu $K_{\alpha 1}$ X-ray source (λ = 1.5406 Å) [11]. With this optics, a good compromise between intensity and resolution requirements could be achieved while obtaining a small divergence angle of the monochromatized beam and a small 2θ-acceptance angle for the diffracted beam.

3.2.1 Determination of lattice mismatch and composition

In XRD experiments, λ and θ are in most cases known. As a result, it is the lattice constant, a, for one or several different crystal orientations that is measured. From this knowledge, not only the strain status of the crystal can be estimated, information about the relative

composition of two or more species in an alloy can also be obtained. This section explains a general way to determine the lattice mismatch, strain and composition.

An epi-layer with another lattice constant than the substrate introduces more lattice points in reciprocal space, slightly shifted from the substrate points. The reciprocal lattice representation is illustrated in Fig. 3.5, indicating the lattice points from a strained (indexed S) and a fully relaxed (indexed R) epi-layer with a larger lattice constant than the substrate. The scattering vectors **G** are the vectors from the origin to the reciprocal lattice points (only **G** to the substrate lattice point is shown in the figure). The axes, $q_{//}$ and $q_{\perp}$, correspond to wave numbers parallel (in-plane) and perpendicular (normal) to the sample surface. Furthermore, ω and ω-2θ directions in reciprocal space are also depicted in the figure, where ω is the angle between **K** and the sample surface.

When the layer is under complete compressive strain, the in-plane lattice constant follows that of the substrate. As a result, the projected parallel vector of the strained layer coincides with that of the substrate, i.e. $q_{//}^{S} = q_{//}^{sub}$. The vector $q_{\perp}^{S}$, however, is reduced compared to the substrate due to the larger lattice constant in the perpendicular direction.

A relaxed epi-layer, on the other hand, has the bulk value of its lattice constant since there is no strain in the material. As the lattice constant is larger in both parallel and perpendicular directions, the magnitude of the projected vectors $q_{//}^{R}$ and $q_{\perp}^{R}$ is reduced compared to the substrate. A fully relaxed epi-layer has a reciprocal lattice point lying on the ω-2θ direction line direction from the substrate reciprocal lattice point.

A two-dimensional map of the reciprocal lattice can be obtained by making many scans in the ω-2θ direction, each of them separated by a small ω-value, $\Delta\omega$. This experimental technique is called reciprocal space mapping (RSM). After projection of the scattering vector into $q_{//}$ and $q_{\perp}$ vectors, the relative lattice mismatch parallel and perpendicular to the surface can be calculated from Eq. 2.3 via

$$f_{//} = \frac{a_{//}^{L} - a_{//}^{S}}{a_{//}^{S}} = \frac{\Delta\left(1/q_{//}\right)}{1/q_{//}^{S}} = \frac{q_{//}^{S}}{q_{//}^{L}} - 1 \tag{3.5a}$$

$$f_{\perp} = \frac{a_{\perp}^{L} - a_{\perp}^{S}}{a_{\perp}^{S}} = \frac{\Delta\left(1/q_{\perp}\right)}{1/q_{\perp}^{S}} = \frac{q_{\perp}^{S}}{q_{\perp}^{L}} - 1 \tag{3.5b}$$

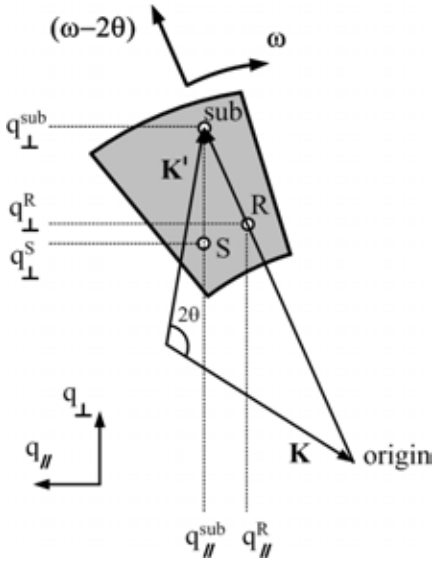

Figure 3.5. Schematic illustration of the Bragg peaks from the substrate (e.g. Si), a strained (S) epi-layer and a relaxed (R) layer (e.g. SiGe).

Herzog proposed that the non-linear variation of the equivalent lattice mismatch as a function of the Ge fraction, *x*, can be determined from [12]

$$f(x) = Ax + Bx^2 \tag{3.6}$$

where $A=3.675\times10^{-2}$ and $B=5.01\times10^{-3}$. Finally, Eqs. 2.5a and 3.6 give a general equation for the Ge concentration

$$x = -\frac{A}{2B} + \sqrt{\left(\frac{A}{2B}\right)^2 + \frac{(f_\perp - f_{//})}{B}\frac{\varepsilon_{//}}{(\varepsilon_{//} - \varepsilon_\perp)} + \frac{f_{//}}{B}} \tag{3.7}$$

3.3 Atomic force microscopy

Uncapped nanostructures are preferably investigated by atomic force microscopy (AFM). There are several advantages of AFM compared to other scanning probe microscopy

techniques, such as scanning tunnelling microscopy (STM); *i)* the sample does not need to be conductive, *ii)* no sample preparation is required, and *iii)* measurements can be carried out in atmospheric ambient. The AFM system used in this work is a commercial NanoScope IIIa (Digital Instruments) with a resolution of ~1 nm in the z-direction and a few nanometers in the x- and y-directions.

Similar to STM, a very sharp tip is scanned across the sample surface, imaging the topography etc. The piezo-electric scanner together with a feedback loop to the software precisely controls the sample movement. The tip could for example be made of Si and it is attached to a cantilever with high spring constant. Short-range forces, such as van der Waal forces and other inter-atomic forces are detected with the tip while scanning. There are three modes in which an AFM can be operated. In the contact mode, the force to the tip is kept constant while the tip is dragged across the surface. Hence, the surface topography is imaged. However, this method can partly destroy the surface since the tip is touching. Therefore, non-contact mode was invented in which the tip-to-sample distance is kept constant. The drawback with this method is that the resolution is lower than in contact mode. Nevertheless, in this work all AFM experiments was performed in the so-called tapping mode. In this mode, the cantilever is oscillating very close to its resonance frequency during scanning. During one oscillation period, which is very short due to the high spring constant of the cantilever, the tip is in contact only for a limited time. This minimizes the damaging of the surfaces while keeping the high resolution. The oscillation amplitude is varying with the average distance between the tip and sample. Large distance implies more space for oscillations and the amplitude increases. With a laser beam reflected on the backside of the cantilever and then detected by a CCD camera, the amplitude is monitored. In this AFM equipment, the feedback control loop adjusts the distance in such a way that the cantilever amplitude remains constant during measurements, and a topographic image is mapped out. From the dedicated software, the lateral and vertical dimensions as well as the shape of the nanostructures (e.g. QDs) can be determined.

3.4 Transmission electron microscopy

Transmission electron microscopy (TEM) is a well-known technique for structural, compositional and chemical characterization of materials [13]. High energetic electrons scattered in a thin specimen can provide images with resolution < 1 nm due to their very short wavelength. Compared to AFM, buried nanostructures (such as QDs and QWs) in a material

can be analyzed. One can divide the microscope into two main parts; the illumination and imaging sections.

In all electron microscopes, the e-gun produces a fine beam of electrons of precisely controlled kinetic energy from a small source region (tip). In so-called field emission gun (FEG) microscopes the tips normally consist of a tungsten wire with a radius of < 100 nm. The electron acceleration voltage is typically ~200 kV. The e-beam is thereafter passing through one or two condenser lenses (coils) with different apertures before it strikes the sample. Microscope alignment involves the centering of the condenser aperture about the optical axis and the elimination of the beam astigmatism.

The most essential part of the imaging section is the objective lens, which controls the image focusing. A diffraction pattern is formed in the back focal plane of the objective lens because all the parallel beams coming from the sample will be focused at one point in this plane. An objective aperture can be inserted here to be able to select the diffraction conditions for imagining, i.e. choosing either the central transmitted beam, which gives a bright field image, or any diffracted (scattered) beam away from the central beam, which gives a dark field image. The diffraction conditions can be selected according to the purpose of the study to be done. An intermediate lens is used to control the magnification.

The TEM equipment used in this work is a FEI Tecnai G^2 UT 200 kV FEG microscope. This is an analytical TEM system, which involves techniques as energy-dispersive X-ray (EDX) spectrometry and electron energy-loss spectrometry (EELS) for chemical and compositional analyzes. In EDX, incident high energetic electrons excite core electrons in the specimen material. When these electrons de-excite, X-rays are emitted and detected. Since the core level energies are fingerprints of the material, the elemental composition can be determined by analyzing the energies and the intensities of the emitted X-rays. The e-beam can be focused to a very small probe of ~1 nm for obtaining high compositional resolution in x-, y-, and z-directions.

In EELS, inelastically scattered electrons are detected to get chemical and compositional information. Energy-loss spectra are characteristic for all materials. However, most of the electrons are normally losing energy by plasmon excitation events. The amount of electrons that are inelastically scattered increases with sample thickness. From the intensity ratio between the zero-loss peak and the peaks from the scattered electrons, it is possible to determine the sample thickness via

$$t = \lambda \ln\left(\frac{I_t}{I_0}\right) \tag{3.8}$$

where I_t and I_0 are the total intensity and the integrated zero loss intensity, respectively. The mean free path, λ, for a plasmon excitation in Si by a 200 keV e-beam is very close to 128 nm [14].

EDX and EELS are normally combined with scanning transmission electron microscopy (STEM). In the STEM mode, electrons elastically scattered from the specimen with high angles are detected, thus providing strong atomic number contrast in the image.

3.5 Photoluminescence

Photoluminescence (PL) is a commonly used technique to get information about the optical and electrical properties of a material, particularly semiconductors. A thermodynamical non-equilibrium situation is created by carrier excitation to higher energy states by an incident light beam to the sample. When these carriers de-excite, they may emit photons with one or several energies, which are detected. The measurements are generally performed at low temperatures in order to minimize phonon scattering and non-radiative processes, which reduces the emission intensity and broaden the luminescence peaks. Excitation above the band gap energy generates carriers, which via fast processes relax through the band structure to states close to the band gap, where the radiative recombination occurs. Thus, PL mainly gives information about the lowest available states, e.g. the band gap energy. There are however related techniques, such as photoluminescence excitation (PLE), in which the excited states can be investigated, but these techniques were not used in these studies.

In the present work, most PL experiments on Si/SiGe nanostructures were performed with an Ar-ion laser (λ = 514 nm) as the excitation source. The wavelength of the emitted light was scanned by a double-grating monochromator and detected by a liquid nitrogen cooled Ge detector. The laser beam was chopped and synchronized with a reference signal, implying that the luminescence signal could be analyzed by standard lock-in technique.

3.6 Detector device fabrication

Successful fabrication of photodetectors requires proper device architecture. In order to make the coupling of the incident light and the absorption efficient, the detector geometry is of

particular importance. Because the device has to be operated under bias condition, metal contacts have to be processed with a low series resistance. In this chapter, some general device fabrication steps are described, which were used in the process flow of the photodetectors produced in this work. A more detailed treatment can be found in ref. [15].

3.6.1 Mask fabrication

Masks are used during photolithography to define the device patterns in different levels. The device layout was designed and drawn in advance with softwares, e.g. Autocad, and then transferred to the masks via a pattern generator. The masks used in this work consist of a 4-inch glass plate with a chromium (Cr) layer and photo resist on one side. In the pattern generator, the resist was exposed by a HeCd laser (λ = 442 nm) according to the pattern design. During exposure, the mask position was accurately controlled and monitored by an interferometer. Line widths down to ~4 µm can be fabricated with our pattern generator. After developing, the unwanted Cr was etched away and the desired pattern was achieved. Several masks had to be prepared for the different levels in a complete process flow. In this case, dedicatedly designed alignment marks were implemented on all masks beside the device patterns.

3.6.2 Photolithography

In the photolithography step, the patterns from the mask were transferred to the sample. First, the sample was coated with photo-resist by spinning for obtaining a homogeneous resist layer. The mask was then placed just above the sample with a small gap distance. With the use of a microscope, the mask was carefully aligned relative to the sample pattern. Thereafter, the sample was lifted directly contacting the mask, followed by the UV light exposure using a Hg lamp (the contact printing mode). The exposure time was typically around 10 s. In the fabrication of the detector devices reported here, only positive photo-resist was used, which implies that it becomes soluble after illumination. In the successive development step, which was carried out with a sodium hydroxide solution, the exposed resist was removed after ~1 minute.

3.6.3 Etching

In the process flow, etching is commonly used to form dedicated structures in the different layers on the Si substrate. Etching can be made either by chemical solutions or by plasma-

enhanced reactive ion etching (RIE). Most of the etching processes remove the material isotropically, which results in under-etching. Therefore, etching is a crucial processing step.

For the fabrication of the QD-based phototransistors in our device process lab, SiO_2 was generally etched by hydrofluoric acid (HF), Al was removed by phosphorous acid for metal lines and contacts, and platinum (Pt) was etched by a solution of so-called King-water (HNO_3:HCl = 1:3). In a few cases, Si was selectively etched by a potassium hydroxide-based (KOH) solution. However, Si and SiGe were in most cases etched by RIE using CF_4/O_2 (5 %) gases for formation of mesa structures. In this process, a Si atom at the surface is bonded to four fluorine atoms, forming SiF_4-gas. Without any bonds to the substrate, the SiF_4 molecule is volatile and can therefore be released from the surface at a minimum of energy. At the same time, the oxygen molecules react with the carbon to produce CO_2. This will release carbon from the surface, which in turn increases the etch rate.

3.6.4 Oxidation

Oxide layers are used in semiconductor devices for various dielectric purposes. SiO_2 can be obtained by three techniques; either by directly oxidizing the Si substrate through a high temperature process in oxygen-rich ambient, by plasma-enhanced chemical vapour deposition (PECVD), or by sputtering.

In the case of thermal dry oxidation, SiO_2 is formed at high temperatures (typically 900-1200°C) through a chemical reaction between Si (from the substrate) and oxygen molecules supplied by the oxygen gas flow. As a result, the SiO_2 is formed at the interface and the amount of Si consumed during the process is about 44 % of the total oxide thickness. Because the O_2 molecules have to diffuse through a SiO_2 layer, the growth rate of SiO_2 decreases with oxide thickness. Due to its high dielectric strength, low densities of traps and defects, and controllable interface states, thermal dry oxide is used as the gate oxide in MOSFETS.

SiO_2 can be deposited at low temperatures through PECVD where the reaction $SiH_4 + N_2O \rightarrow SiO_2$ forms the oxide layer. In fact, most SiO_2 depositions implemented in the process flow of our detector devices were made by PECVD. The main reason was to avoid the high temperatures needed for the thermal oxidation process, which would be detrimental for the device performance by means of lattice relaxation and Si-Ge alloying. The PECVD technique only requires ~300 °C during deposition. The poor oxide quality was usually compensated by the growth of a relatively thick gate oxide layer, followed by an annealing procedure to remove residual hydrogen atoms and to dense the layer.

3.6.5 Metallization

All metallization in this work was performed by magnetron sputtering. This technique gives better adhesion and step coverage than, for example, metal deposition by thermal evaporation. Sputtering took place in a vacuum chamber with a background of Ar gas, while the metal target was negatively biased. During operation, Ar^+ ions generated through the Ar plasma move towards the target with high enough energy to "kick out" target material. High-energy metal atoms from the target reach the sample and deposition occurs.

In general, Al was used for the metal contacts, and for some photodetectors Pt was also sputtered to form the gate contact.

3.7 Photoconductivity measurements

In photoconductivity measurements, incident light on the photodetectors generates a photocurrent that is measured under certain bias conditions. In the present work, most of the measurements were performed with InGaP/InAs quantum well laser modules at 1.31 and 1.55 μm as light sources. The light beam was incident to the detectors via an optical fiber. The power and spot size were carefully calibrated, in order to achieve accurate photoresponsivity results. Fig. 3.6 shows the output optical power as a function of laser current together with a normalized intensity profile of the beam.

A resistor was connected in series with the detector device. Parallel to the resistor, a lock-in amplifier was connected. Using a square-pulsed laser beam incident on the photodetectors, the photocurrent was measured by the lock-in equipment, which subtracts the dark current. Actually, it is the voltage increase over the resistor, due to the photo-induced current, that is measured. For three-terminal photodetectors, a separate external power supply was used for the gate bias. Photocurrent measurements were performed both with light incident from the normal direction and from the edge of the devices. The total current and the voltage across the detector were also monitored.

For spectroscopic photoconductivity measurements, a calibrated tungsten halogen lamp was used in front of a monochromator for wavelength selection and a set of lenses to focus the light beam. Time-resolved measurements of the photocurrent was carried out by a TDS 620B digital real-time oscilloscope, which was connected in parallel to the resistor.

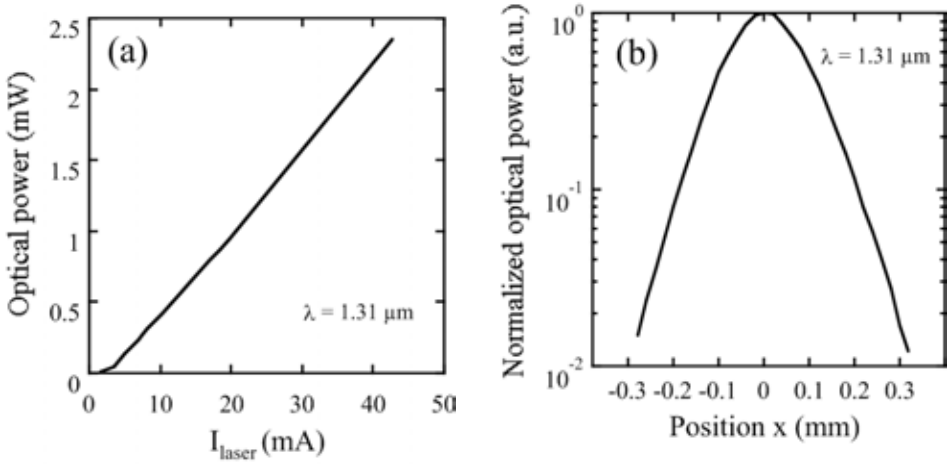

Figure 3.6. Laser characteristics, necessary for precise photoconductivity measurements. The optical laser power dependence of the bias (a), and the normalized intensity profile of the laser beam (b).

The photoresponsivity, defined as the ratio between the generated photocurrent and the incoming optical power, was calculated from

$$R_{resp} = \frac{V}{P_{op} R} C \tag{3.9}$$

where R is the resistance, V is the photo-induced voltage across the resistance, P_{op} is the optical power and C is a coupling factor that takes the geometry losses into account.

References

[1] H. Roth, *Vacuum technology*, North-Holland, Amsterdam, 1986.

[2] J. A. Venables, Surf. Sci. **299/300**, 798 (1994).

[3] F. Allen and E. Kasper, "Models of silicon growth and dopant incorporation" in " Silicon molecular beam epitaxy" ed. E. Kasper and J. C. Bean (CRC Press, Florida, 1988) vol 1, ch.4.

[4] R. L. Headrick, B. E. Weir, J. Bevk, B. S. Freer, D. J. Eaglesham, and L. C. Feldman, Phys. Rev. Lett. **65**, 1128 (1990).

[5] H. P. Zeindl, T. Wegehaupt, I. Eisele, H. Oppolzer, H. Reisinger, G. Tempel, and F. Koch, Appl. Phys. Lett. **50**, 1164 (1987).

[6] A. A. van Gorkum, K. Nakagawa, and Y. Shiraki, Jpn. J. Appl. Phys. **26**, L1933 (1987).

[7] R. A. A. Kubiak, W. Y. Leong, and E. H. C. Parker, Appl. Phys. Lett. **46**, 565 (1985).

[8] H. Jorke, H.-J. Herzog, and H. Kibbel, Appl. Phys Lett. **47**, 511 (1985).

[9] W.-X. Ni, J. Knall, M.-A. Hasan, G. V. Hansson, J. E. Sundgren, S.A. Barnett, L. C. Markert, and J. E. Greene, Phys. Rev. B **40**, 10449 (1989).

[10] W.-X. Ni, J. O. Ekberg, K. B. Joelsson, H. H. Radamson, A. Henry, G.-D Shen, and G. V. Hansson, J. Cryst. Growth, **157**, 285 (1995).

[11] W.-X. Ni, J. Birch, Y.S. Tang, K.B. Joelsson, C. Sotomayor-Torres, Å. Kvick, and G.V. Hansson, Thin Solid Films, **294**, 300 (1997).

[12] H.-J. Herzog, Solid State Phenomena **32-33** 523 (1993).

[13] D.B. Williams and C.B. Carter in (1996) *Transmission Electron Microscopy*, p.600, Plenum Press, New York.

[14] Y. Uchida, O. Spillecke, G. Lehmpfuhl, A. Preusser, K. Weiss, and R. Schlögl, Cryst. Res. Technol. **34**, 103 (1999).

[15] S. A. Campbell, *The Science and Engineering of Microelectronic Fabrication*, 2nd edition, Oxford University Press, New York (2001).

Chapter 4

Si/SiGe photodetectors

As mentioned in chapter 2, optical components based on group-IV materials are of particular interest due to the possibility to integrate them with well-established Si microelectronics. There are several advantages of using Ge QDs incorporated into the Si matrix. The band gap energy of pure Ge corresponds to the near-infrared wavelength range, which is used in the fiber optical communication systems. The most established and simplest way to implement dislocation free Ge in Si is via the formation of islands in the Stranski-Krastanov growth mode. Furthermore, the quantum confinement effects (also discussed in chapter 2) in the QDs enhance the no-phonon optical transition probability.

4.1 General description of a semiconductor photoconductor

This section will deal with the simplest type of photodetector; namely the photoconductor [1]. A photoconductor is an intrinsic semiconductor with two ohmic contacts for application of an external bias. Light incident to the photoconductor will generate electron-hole pairs in the semiconductor material if the photon energy is larger than the band gap energy. The generated carriers are then driven by the applied electric field, resulting in a photocurrent.

Assume that a constant flux of photons is incident to the photoconductor at zero bias. The total number of photons arriving to the sample surface per unit time is

$$N_{photon} = \frac{P_{op}}{h\nu} \tag{4.1}$$

where P_{op} is the optical power, h is Plancks constant and ν is the frequency of the oscillating electromagnetic wave. The number of electron-hole pairs generated by each photon is called internal quantum efficiency and is described as

$$\eta_{\text{int}} = \frac{I_{ph}^{'}}{qN_{photon}} = \left(\frac{I_{ph}^{'}}{q}\right)\left(\frac{h\nu}{P_{op}}\right) \Rightarrow I_{ph}^{'} = q\left(\eta_{\text{int}}\frac{P_{op}}{h\nu}\right) \tag{4.2}$$

$I_{ph}^{'}$ is the primary photocurrent (generated only by the incoming photons) and q is the elementary charge. The quantum efficiency is strongly dependent on the absorption coefficient, α. Assuming that all photons are absorbed in the material, the carrier generation rate per unit volume can be expressed by

$$G = \frac{\eta_{\text{int}}}{V}N_{photon} = \frac{\eta_{\text{int}}}{V}\left(\frac{P_{op}}{h\nu}\right) \tag{4.3}$$

where V is the volume in which the carriers have been generated. However, the carriers have an average lifetime, τ, before they recombine. As a result, the number of carriers decays with time, t, if the illumination is turned off. This can be written as

$$n(t) = n_0 \exp\left(-\frac{t}{\tau}\right) \tag{4.4}$$

In turn, the carrier recombination rate is given by

$$\left|\frac{dn}{dt}\right| = \frac{1}{\tau}\exp\left(-\frac{t}{\tau}\right) = \frac{n}{\tau} \tag{4.5}$$

During normal operation, a steady state situation will occur where the generation rate is equal to the recombination rate.

$$\frac{n}{\tau} = \frac{\eta_{\text{int}}}{V}\left(\frac{P_{op}}{h\nu}\right) \Rightarrow n = \frac{\eta_{\text{int}}\tau}{V}\left(\frac{P_{op}}{h\nu}\right) \tag{4.6}$$

The total photocurrent depends on *n* via

$$I_{ph} = qnv_d A = q\left(\eta_{\text{int}}\frac{P_{op}}{h\nu}\right)\left(\frac{\tau v_d}{L}\right) \tag{4.7}$$

with the use of Eq. 4.6 and the fact that the distance, *L*, between the electrodes with area A is simply *V/A*. v_d is the carrier drift velocity. The carrier transit time is the time that takes for the carriers to travel between the electrodes, and is defined as $t_r = L/v_d$. Thus Eq. 4.7 becomes

$$I_{ph} = q\left(\eta_{\text{int}}\frac{P_{op}}{h\nu}\right)\left(\frac{\tau}{t_r}\right) \tag{4.8}$$

Eq. 4.8 expresses the total photocurrent. Comparing this with the primary photocurrent given by Eq. 4.2, we can determine the current gain using

$$Gain = \frac{I_{ph}}{I_{ph}^{'}} = \frac{\tau}{t_r} \tag{4.9}$$

In other words, Eq. 4.9 tells simply that there is a possibility to achieve a photocurrent gain that is substantially greater than unity, if the minority carrier lifetime is very long while the geometrical design leads to a short transit time, i.e. a large number of carriers can reach the metal contacts before they experience recombination events.

Several issues are important when achieving a gain value > 1. Firstly it is necessary to reduce the probability for recombination, therefore, efficient carrier separation is crucial. Consider a biased photoconductor where an electron reaches the contact leaving a hole within the specimen volume. As an example, a potential barrier may trap the hole. Instantly, a positive charge is built up in the sample. An electron in the contact can be attracted by this charge and will move into the active region. However, with a low recombination rate, there is a high probability that the electron reach the other electrode. If the hole is still within the specimen, another electron can pass between the contacts and so on. Therefore, more than one

electron can contribute to the current for each generated hole. The result is the photocurrent gain effect described by Eq. 4.9.

Secondly, a high drift velocity is also needed. v_d is proportional to the carrier mobility, μ, which in the case of Si/SiGe can be enhanced by introducing strain in the material, as was discussed in section 2.1.

Thirdly, the speed of the photoconductor is another important property that has to be taken into consideration. When the incident light power is turned off, the decrease in photocurrent with time approximately follows Eq. 4.4. A long carrier lifetime results in a slow decay and the speed of the photoconductor will be reduced. Consequently, the photocurrent, described by Eq. 4.8, and the device speed are competing properties and have to be balanced in order to obtain a suitable detector for a certain application.

4.2 Ge/Si quantum dot photodetectors

In this work, we have focused on Ge dot photodetectors working in the near-infrared range, i.e. the photon absorption occurs via inter-band excitations. This section will therefore mainly consider Ge/Si island devices fabricated for light detection at 1.3-1.55 μm. Also as an important application aspect, a brief description of the mid- and far-infrared photodetectors based on the inter-subband transitions in Ge dots will be given in this section.

4.2.1 Near-infrared Ge dot photodetectors

Near-infrared light has a corresponding photon energy, $h\nu$, that is $E_{gGe} < h\nu < E_{gSi}$, which means that the photons only interact with the Ge islands and not with the surrounding Si. Fig. 4.1 schematically shows two possible inter-band absorption events when light is incident to an intrinsic Ge/Si QD detector device. Since the band gap energy of Ge is much larger than k_BT at 300 K, this type of detector can be operated up to room temperature. The notch potentials in the conduction band of Si are due to the tensile strain that splits the energy bands. Since the band alignment is of type II, there can be both spatially indirect and direct excitations in real space, as depicted in the figure. Due to Si-Ge alloying and quantum confinement effects, the condition of k-conservation is relaxed and these transitions can occur without phonons. To work as a detector, it is very important to enhance transport of the excited carriers, i.e., the generated holes should contribute to the photocurrent by escaping from the potential well either by thermal emission or by field emission when a sufficient bias is applied. The photon

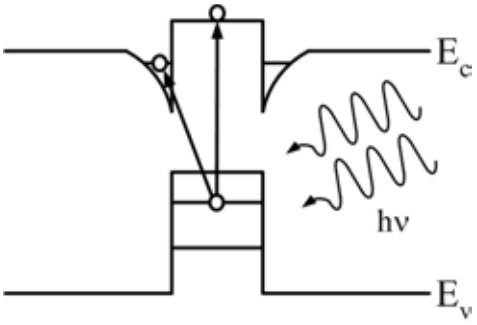

Figure 4.1. Schematic drawing of the potential band diagram showing the spatially direct and indirect excitation events.

absorption will also be enhanced if several Ge dot layers are incorporated in the Si matrix, leading to an increased absorption volume.

The most studied Ge/Si QD photodetectors are based on p-i-n photodiode structures with the island layers embedded in the intrinsic region, as illustrated in Fig. 4.2 [2-8]. In these structures it is easier to form ohmic electrodes by fabrication of highly doped contact layers in direct connection to the junction. The p-i-n type of QD diode has several advantages. The dark current is very low since it is normally operated under reverse bias. Moreover, there is a built-in electric field that facilitates the carrier separation process. In principle, the device can be operated like a solar cell, i.e. without applying an external voltage. However, by applying a reverse bias the photo-generated carriers are more efficiently separated and the photocurrent is expected to increase by some amount. Low escape probability and re-capturing of holes in subsequent dot layers during transport is in general believed to be a problem, in particular at low bias due to the relatively short lifetime [9]. Trapped holes in an island may also have enhanced recombination probability with an electron, possibly via the Ge/Si interface. Hence, the reported photo-response values in the literature of this type of detectors were not very high, and no photocurrent gain effect described by Eq. 4.9 has ever been reported.

Assuming no current gain and normally incident light, a theoretical expression of the responsivity can be written as [10]

$$R_{resp} = \frac{\lambda}{1.24}\left(1-\Theta_R\right)\eta_{\text{int}}\left(1-\exp\left(-\alpha W\right)\right) \qquad (4.10)$$

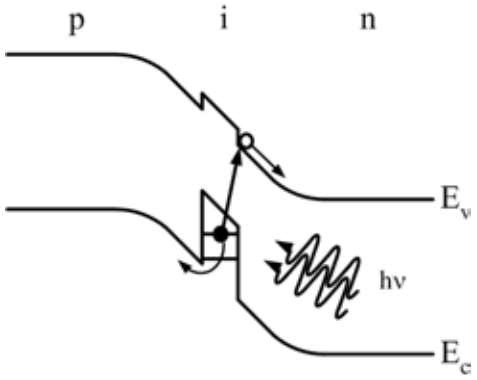

Figure 4.2. Working principle of a Ge dot p-i-n photodiode.

where λ is the wavelength (in vacuum) of the incident light measured in μm, Θ_R is the reflectivity and W is the thickness of the active region. η_{int} and α are defined in section 4.1. The reflectivity is around 0.3 for near-infrared light incident normal to the Si surface (~30 % of the optical power is reflected without penetrating the detector device) [11]. The factor 1-exp(-αW) is simply the fraction of photons absorbed in the active region. Assuming that the reflectivity and absorption volume can be increased such that Θ_R = 1 and αW is infinitely large, the maximum theoretical photo-responsivity value is λ/1.24. This corresponds to about R_{resp}= 1.05 A/W at 1.31 μm and R_{resp}= 1.25 A/W at 1.55 μm, respectively. Even though this situation may not be achieved in practice, it is possible to increase the detector performance by optimizing Θ_R, η_{int} and αW. As an example, antireflection coatings can reduce the reflectivity.

The αW product is however relatively small for a Ge/Si QD detector designed for normal incidence light absorption. One photon can only pass through maximum one island in each dot layer, as shown in Fig. 4.3 (A). If the number of island layers is not sufficiently large, a significant fraction of the incoming photons would penetrate through the device (there is no interaction with Si). This can be compensated by using waveguide geometry, e.g. to couple the light through the edge of a rib-type detector device with a long-enough optical path allowing propagation of photons parallel to the QD layers, as illustrated in Fig. 4.3 (B). From the fact that a typical island density is 10^8-10^{11} cm^{-2}, it is obvious that the absorption volume is increased and each photon will have the possibility to interact with several Ge dots in one QD layer. For the case of edge incidence, the theoretical expression for the photo-responsivity is similar to Eq. 4.10, but with an additional coupling efficiency constant, similar to that in

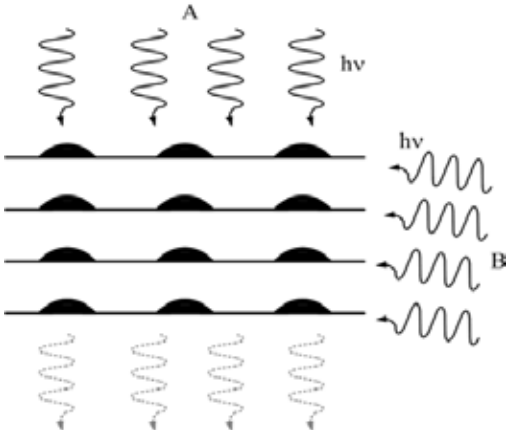

Figure 4.3. Illustration of the normal (A) and edge (B) incidence geometries.

Eq. 3.9. The enhanced absorption volume is explained by an increased *W*, which is comparable to the length of the device and therefore much larger than the active region thickness in a detector designed for normal incidence.

A complete design of a Ge dot waveguide photodetector should contain a high-refractive index material (e.g. SiGe) next to the active region, which confines the optical modes close to the dot layers. The detector efficiency can then be further improved, and typical examples are reported in Ref. 5 and 6.

There are other methods to enhance the detector performance. As mentioned before, Eq. 4.10 does not include any photocurrent gain. In phototransistors, there is an amplification of the photo-generated current, which can raise the stated quantum efficiency to a value larger than unity. The QD near-infrared phototransistors reported in this thesis work were based on two detector structures, namely a heterojunction bipolar phototransistor (HBT) and a three-terminal lateral FET type of detector. The photocurrent gain effect in the HBT will be discussed in chapter 6. On the other hand, from section 4.1 we remind that any gain in photocurrent in the lateral FET phototransistor can only be ascribed to Eq. 4.9.

4.2.2 Mid- and far-infrared Ge dot photodetectors

The transition energies required for mid- or far-infrared light absorption are in the 10 – 500 meV range, which fit with inter-subband transitions in Ge/Si QD systems [12-17]. In practice, the photodetector devices are fabricated using hole inter-subband effects in the Ge dots because of the favored band offset in the valence band. Accordingly, p-type doping is

required inside or next to the islands. The most commonly used dopant is B, which has an impurity level just ~50 meV from the valence band edge. Thus, a considerably amount of the B atoms are ionized even at low temperatures. Doping next to the island layers has the advantage of reducing influence from ionized charges and impurity levels inside the QDs. The holes are thermally excited into the Si valence band and thereafter trapped in the islands. A low operation temperature is often required in order to minimize thermal emission of the holes out of the Ge dots, which otherwise increases the dark current and decreases the photo-response significantly, since that reduces the number of holes to be excited [18]. Typically a mid- or far-infrared detector operates below the liquid nitrogen temperature of 77 K.

Photon absorption in the far-infrared range typically involves hole excitation from the ground state to an excited state in the Ge island, followed by hole transport to the contact by an applied voltage. The tunneling process is more important for far-infrared detectors because of the low operation temperature, unless the excited state is very close to the Si valence band edge (in the order of k_BT). The dots have to be designed properly (size, shape etc.) so there is at least one excited state available. The doping concentration is also crucial. A low number of holes in the dots reduces the response, while too many holes leads to an increased occupation probability of the excited states. In the mid-infrared photon energy range, the detectors are often designed in utilizing bound-to-continuum hole excitations where light with somewhat higher energy is incident to the Ge QD absorbing region.

Mid- and far-infrared dot detectors are unipolar devices, where only one type of carrier (holes) conducts the photocurrent. According to Eq. 4.9, it seems to be possible to obtain a high current gain, because once a hole has moved out from the potential well, the remaining negatively charged ionized B atom may generate the built-in field in the active region, resulting in the same effect as described above. In practice, the situation could be more complex, since such charged centers could enhance the re-trapping mechanism owing to Coulombic interactions. It would therefore reduce the measured photocurrent and quantum efficiency. Hence, it is important to minimize the recapture effect in these detector structures.

References

[1] S. M. Sze, *Semiconductor devices: Physics and Technology*, 2nd edition, published by John Wiley & Sons Inc. 2002.

[2] S. Tong, J.-L. Liu, J. Wan, R. Faez, V. Pouyet, and K. L. Wang, Proceedings of SPIE - The International Society for Optical Engineering **4580**, 193 (2001).

[3] M. Elkurdi, P. Boucaud, S. Sauvage, O. Kermarrec, Y. Campidelli, D. Bensahel, G. Saint-Girons, and I. Sagnes, Appl. Phys. Lett. **80**, 509 (2002).

[4] J. Wan, S. Tong, Z. Jiang, G. Jin, Y. H. Luo, J.-L. Liu, X. Liao, J. Zou, and K. L. Wang, Proceedings of SPIE - The International Society for Optical Engineering **4656**, 89 (2002).

[5] M. Elkurdi, P. Boucaud, S. Sauvage, G. Fishman, O. Kermarrec, Y. Campidelli, D. Bensahel, G. Saint-Girons, G. Patriarche, and I. Sagnes, Physica E **16**, 450, (2003).

[6] M. Elkurdi, P. Boucaud, S. Sauvage, G. Fishman, O. Kermarrec, Y. Campidelli, D. Bensahel, G. Saint-Girons, G. Patriarche, and I. Sagnes, Physica E 16, 523 (2003).

[7] A. Alguno, N. Usami, T. Ujihara, K. Fujiwara, G. Sazaki, and K. Nakajima, Appl. Phys Lett. **83**, 1258 (2003).

[8] A. Alguno, N. Usami, T. Ujihara, K. Fujiwara, G. Sazaki, K. Nakajima, K. Sawano, and Y. Shiraki, Appl. Phys. Lett. **84**, 2802 (2004).

[9] K. Brunner, Rep. Prog. Phys. **65**, 27 (2002).

[10] L. Colace, G. Masini, and G. Assanto, “Silicon Heterostructure Handbook” edited by John Cressler, Taylor & Francis, Boca Raton, 2006, ch. 7.3, pp. 731.

[11] E. Barta, and G. Lux, J. Phys. D: Appl. Phys. 16, 1543 (1983).

[12] A. I. Yakimov, A. V. Dvurechenskii, Yu. Yu. Proskuryatov, A. I. Nikiforov, O. P. Pchelyakov, S. A. Teys, and A. K. Gutakovskii, Appl. Phys. Lett. **75**, 1413 (1999).

[13] A. V. Dvurechenskii, I. A. Ryazantsev, A. P. Kovchavsev, G. L. Kuryshev, A. I. Nikivorov, and O. P. Pchelyakov, Proceedings of SPIE - The International Society for Optical Engineering **5126**, 167 (2002).

[14] D. Bougeard, K. Brunner, and G. Abstreiter, Physica E **16**, 609 (2003)

[15] S. Tong, F. Liu, A. Khitun, and K. L. Wang, J. Appl. Phys. **96**, 773 (2004).

[16] S. Tong, J.-Y. Lee, H.-J. Kim, F. Liu and K. L. Wang, Optical Materials **27**, 1097 (2005).

[17] S. Tong, H.-J. Kim, and K. L. Wang, Appl. Phys. Lett. **87**, 081104 (2005).

[18] L. Chu, A. Zrenner, D. Bougeard ., M. Bichler, G. Abstreiter, Physica E **13**, 301 (2002).

Chapter 5

Fundamental study of Si/SiGe nanostructures

The electrical and optical properties of Si/SiGe nanostructures are dependent on their size, shape, strain, and material composition. The growth parameters have to be well-established in order to fulfill the requirements of a Si/SiGe photodetector, specifically designed for certain applications. This chapter will mainly focus on the material characterization of Si/SiGe nanostructures, which is an important part in order to facilitate a proper design of efficient phototransistors.

5.1 Size, shape and density of Ge islands

It was already discussed in chapter 2 that the optical properties of the Ge dots are modified by the size of the islands since the carrier quantum confinement is dependent on the structural dimensions. The energy band structure in a Ge QD system becomes even more complex if the dot shape is taken into account.

5.1.1 Growth rate dependence

The size, shape and density of Ge islands in a single dot layer deposited on a Si(100) substrate is mainly dependent on three growth parameters; substrate temperature, growth rate, and the amount of Ge deposited. The growth rate has to be drastically varied in order to see any substantial difference in dot size. Capellini et. al. demonstrated a ~30 % reduction of the

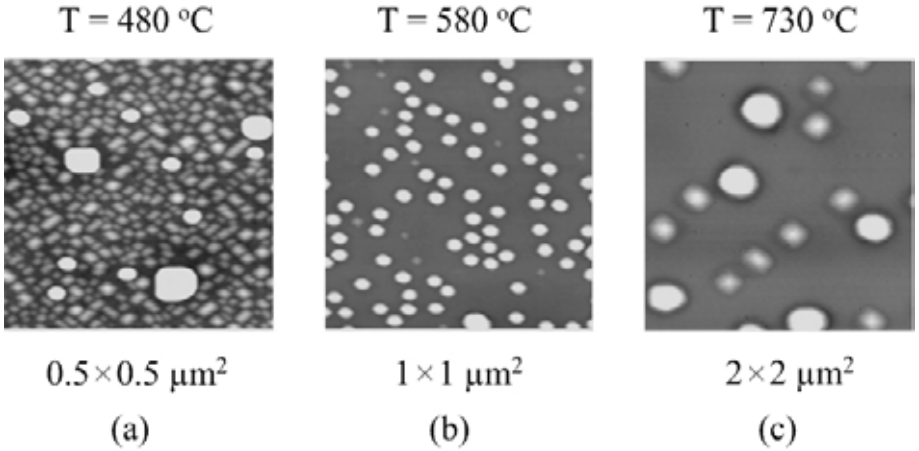

Figure 5.1. Tapping mode AFM images of uncapped Ge island grown at 480 °C (a), 580 °C (b), and 730 °C (c). The island dimensions are increased with temperature. Observe the different scales for the three figures.

island lateral dimension by increasing the deposition rate from 4 mono-layers (ML) per minute to 40 ML/min [1]. This is due to the fast increase in ad-atom concentration on the surface, resulting in an enhanced island nucleation probability. A high growth rate simply implies that the Ge atoms have less time to rearrange to form larger islands. Since the same amount of material is deposited in the two cases, an increased island density compensates the reduced island size.

5.1.2 Growth temperature dependence

The growth temperature also influences the island size. The substrate temperature is typically 400-750 °C during dot fabrication. At low deposition temperatures, the diffusion length of the ad-atoms is limited and the islands are small in size with a high density. Oppositely, the dots become larger at elevated temperatures due to the longer diffusion length [2]. The large amount of material in these islands requires a reduction of the dot density. The enhanced diffusion length also involves more Ge transport into the islands, resulting in a thinner WL.

Fig. 5.1 shows AFM images of uncapped Ge islands grown at three substrate temperatures. In the growth experiment, nominally 8 ML of Ge was deposited. It is evident that the increase of dot size is accompanied with the reduction in dot density when increasing the growth temperature (observe the different scales in the figure). The temperature dependence of the dot density and average lateral size is summarized in Fig. 5.2 for a set of samples based on AFM measurements.

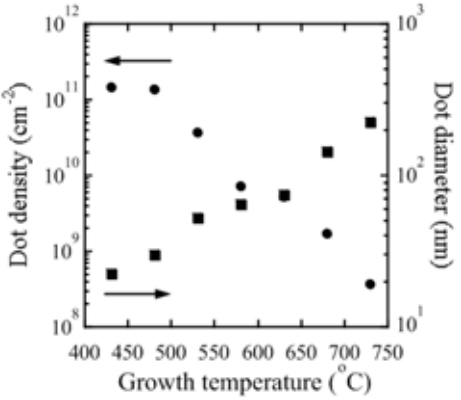

Figure 5.2. The Ge dot density (circles) and the average island diameters (squares) as a function of growth temperature.

Fig. 5.1 also shows islands with different shapes. At low temperatures the QDs are typically so-called hut clusters with {105} facets [3,4]. These can be elongated in the [010] direction and even form a 90° angle. QDs grown at higher temperatures have a round shaped base area and are called dome clusters. In general, a dome cluster QD reveals multi-facets. It has been established that these are mainly in the {113} directions, but also facets in {210}, {221} and {320} directions have been demonstrated [2]. Furthermore, pyramid shaped Ge islands of different sizes have been observed in the entire growth temperature range [5]. As shown in Fig. 5.1c, the pyramids are considerably smaller in size than the round shaped dome clusters.

5.1.3 The effect of Si overgrowth

Si capping modifies the shape and dimensions of the Ge QDs [6,7]. It has been demonstrated that larger dome sized islands transform into pyramids during the initial stage of overgrowth [7-9]. It has however been reported that there is a pyramid-to-dome transition as the capping proceeds [10]. The hut clusters are generally less influenced by capping [8]. Fig. 5.3 are STEM images revealing the difference between an embedded and surface Ge dot grown at 630 °C. While the lateral dimensions are only slightly increased, the height is significantly reduced after capping. Hence, there is a redistribution of Ge material during overgrowth. However, the influence of Si overgrowth also depends on the substrate temperature and other growth parameters.

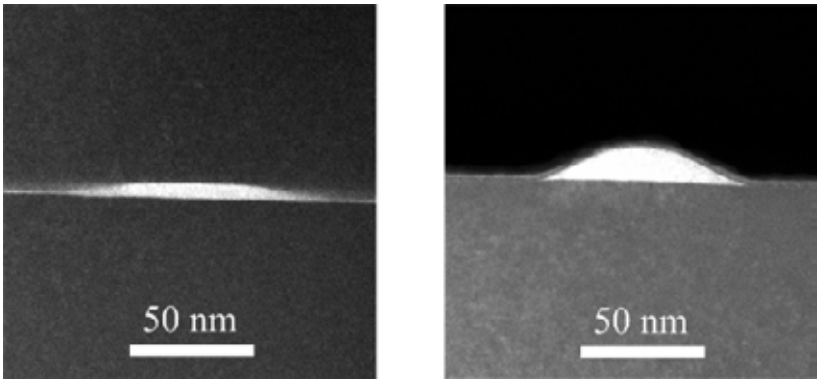

Figure 5.3. Capped and uncapped islands grown at 630 °C. The change in height is most significant, it is reduced by a factor of >2 during overgrowth.

5.2 Composition in $Si_{1-x}Ge_x$ islands

Up until now the islands have been referred to as Ge QDs. In fact, it is well known that a substantial intermixing of Si and Ge occurs during the growth process, leading to $Si_{1-x}Ge_x$ alloyed islands. Material composition is strongly linked with strain, and both properties determine the band gap energy, as discussed in section 2.2. Intermixing is energetically favorable since it reduces the total strain energy in the system [11]. Actually, the compositional dependence of the ground state energy was suggested to dominate over the confinement shift, except for the extremely small islands [12,13]. The strain plays an important role for the growth and alloying process. Strain-enhanced Si-Ge inter-diffusion was observed by Schmidt et. al. [14] and U. Denker et. al. [15]. Furthermore, Ge islands grown by CVD revealed a reduced intermixing, particularly at low temperatures, compared to dots fabricated by MBE [16,17]. This was attributed to the hydrogen-rich surface, which prevented Si diffusion into the QDs below 550 °C during CVD epitaxial growth.

The alloying is mainly thermally activated and therefore strongly dependent on the substrate temperature during growth. Thus, the increased size of Ge islands with temperature is not only due to the enhanced Ge diffusion length, but also a result of the significant Si-Ge intermixing. Most compositional studies have been based on analyses of uncapped islands [16-25]. However, it is more interesting to analyze capped $Si_{1-x}Ge_x$ QDs, since these are relevant for application purposes. It has been proposed that the Si-Ge alloying is enhanced during Si overgrowth [13,26]. An example is shown in Fig. 5.4, where a drift-corrected EDX line scan reveals a slightly sharper Si/Ge interface at the bottom of the island than above. The

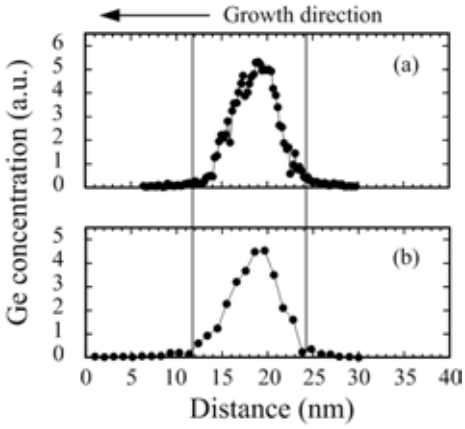

Figure 5.4. Vertical Ge profiles across Ge islands grown at 630 °C (a), and 680 °C (b), measured by drift-corrected EDX. A slightly sharper Ge/Si interface is revealed underneath the island. A larger height of the island in (b) is also observed.

extra contribution to the intermixing during Si capping is ascribed to the Ge segregation effect during the initial stage of capping, since Ge has lower dangling bond and surface energy than Si [27].

Fig. 5.5 depicts the temperature dependence of the atomic composition inside $Si_{1-x}Ge_x$ QDs [28]. The results were extracted from a combination of several measurement techniques, including STEM, EDX and EELS. A special sample preparation procedure was implemented in order to obtain thin specimens with slowly varying thicknesses so the Cliff-Lorimer relation was valid for calculating the Ge fraction [29]. From the zero loss and plasmon peaks revealed from the EELS experiments, the sample thickness at the island position was determined by Eq. 3.8. The larger islands grown at higher temperatures could be directly quantified from EXD by analyzing the Si and Ge K_α X-ray peaks since the dots occupy the entire specimen volume. The determination of the Ge concentration becomes less accurate for small islands. Ge islands smaller than 50 nm in diameter were normally only occupying part of the sample thickness and the excess Si-K_α X-ray signal has to be taken into account. The reduced Ge fraction at higher deposition temperatures is interpreted as enhanced Si-Ge alloying. However, the reduction is slower for temperatures above ~600 °C. This can be explained by the longer distance between the Si/Ge interface and the core of the larger sized dome-shaped islands, leading to a limited amount of Si atoms reaching the dot center. This is in agreement with PL experiments performed on the same structures [12].

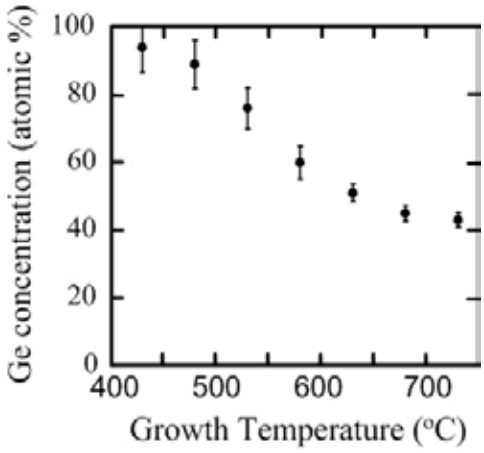

Figure 5.5. Ge concentration inside the islands as a function of growth temperature. The measurements were performed directly with EDX or combined with EELS.

In the following sections, the notation Ge QDs will still be referred to the $Si_{1-x}Ge_x$ alloyed islands.

5.3 Vertical alignment of Ge islands

To increase the probability of light absorption in a photodetector, the absorption volume has to be large, which was shown by Eq. 4.10. Hence, several Ge island layers are preferably incorporated in the structure. In this case, Si has to be deposited to separate each dot layer. As mentioned in chapter 2, the Si above the Ge islands is tensely strained due to the partially elastic relaxation within the dots. If the layers are pseudomorphic, there must be an amount of compressive strain in the region between the QDs [11,30]. As a result, positions right above the buried islands are energetically favorable sites for nucleation of new Ge islands in the next dot layer. Vertical columns of Ge QDs are therefore formed in multi-stack island layers. However, if the Si spacer layers have a thickness that is comparable or larger than the dot diameter, the strain fields are compensating each other at the surface, leading to a reduced correlation between the QD layers. A typical example is shown in Fig. 5.6 illustrating TEM images of two Ge dot samples with Si spacer layer thicknesses of 17 nm (a) and 60 nm (b). Even though the average dot size is somewhat smaller in (a), there is a correlation between the island layers resulting in the vertical column, while the strain field is smeared out in the thick spacer layer sample leading to randomly distributed Ge islands.

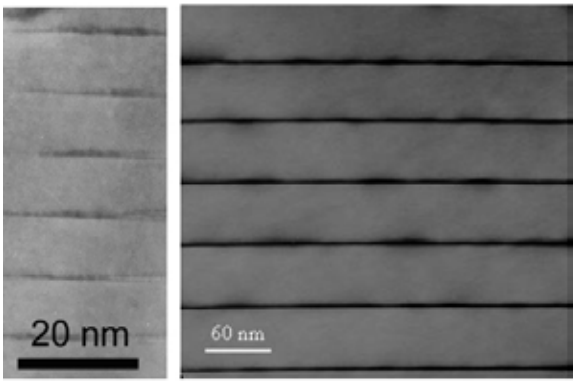

Figure 5.6. TEM images of two Ge dot samples with Si spacer layer thicknesses of 17 nm (a) and 60 nm (b). Vertical alignment can only be observed when the Si spacer layer thickness is comparable or smaller than the dot diameter, which is the case in (a).

5.4 Si/SiGe(110)

$Si_{1-x}Ge_x$ grown on Si(110) is a new hetero-material system that has recently revealed several interesting and promising features for some applications in electrical and optical devices, such as photodetectors. It has been shown that the strain-enhanced hole mobility in Si(110), pseudomorphically grown on SiGe, is larger than that in strained Si(100) [31]. High electron mobility has also been demonstrated, which makes the Si/SiGe(110) material system to a potential candidate for future CMOS technology [32]. Moreover, fabrication of waveguides is facilitated due to the {111} cleavage planes, which are normal to the (110) surface.

Ge islands can also be fabricated on Si(110) [33,34]. With proper composition and strain conditions, it is predicted that the band alignment of these islands is of type I [35-37]. With both electrons and holes confined within the Ge QD, the probability for optical transitions would increase. A proper photodetector could be designed with several Ge(110) island layers sandwiched between SiGe 2D layers in order to confine the light.

However, this material system has not been extensively studied. The thermal stability of metastable SiGe/Si(110) 2D layers has to be completely understood. High power consumption during operation increases the device temperature, which can activate unwanted nucleation and propagation of dislocations. Unlike the (100) surface, the (110) surface has two perpendicular in-plane directions that are of importance, i.e. $[\bar{1}10]$ and [001]. Hence, the relaxation may not be symmetric in all directions. To get information about the strain

condition for the two crystallographic orientations, RSM experiments have to be carried out around at least two reciprocal lattice points. For example, mapping around the (260) lattice point gives the mismatch along in-plane [$\bar{1}$10] and perpendicular [110] directions, while information about the in-plane [001] lattice mismatch can be obtained from RSM measurements around the (062) lattice point. Some results about the strain and the materials thermal stability of SiGe/Si(110) heterostructures are discussed in paper VII.

References

[1] G. Capellini, M. De Seta, and F. Evangelisti, J. Appl. Phys. **93**, 291 (2003)

[2] S. A. Chaparro, Y. Zhang, Jeff Drucker, D. Chandrasekhar, and D. J. Smith, J. Appl. Phys. **87**, 2245 (2000)

[3] Y.-W. Mo, D. E. Savage, B. S. Swartzentruber, and M. G. Lagally, Phys. Rev. Lett. **65**, 1020 (1990).

[4] Martin Kästner, and Bert Voigtländer, Phys. Rev. Lett. **82**, 2745 (1999).

[5] G. Jin, J. L. Liu, K. L. Wang, Appl. Phys. Lett. **83**, 2847 (2003).

[6] M. Kummer, B. Vögeli, and H. von Känel, Materials Science and Engineering B **69**, 247 (2000).

[7] O. Kirfel, E. Müller, D. Grützmacher, and K. Kern, Physica E **16**, 602 (2003).

[8] O. Kirfel, E. Müller, D. Grützmacher, K. Kern, A. Hesse, J. Stangl, V. Holý, and G. Bauer, Appl. Surf. Sc. **224**, 139 (2004).

[9] A. Rastelli, M. Kummer, and H. von Känel, Physica E 13, 1008 (2002).

[10] V. Yam, V. Le Thanh, D. Débarre, Y. Zheng, and D. Bouchier, Appl. Surf. Sc. 224 143 (2004).

[11] O. G. Schmidt and K. Eberl, Phys. Rev. B **61**, 13721 (2000).

[12] M. Larsson, A. Elfving, W.-X. Ni, G. V. Hansson, and P.-O. Holtz, submitted to Phys. Rev. B.

[13] M. Stoffel, U. Denker, G. S. Kar, H. Sigg, and O. G. Schmidt, Appl. Phys. Lett. **83**, 2910 (2003).

[14] O. G. Schmidt, U. Denker, S. Christiansen, and F. Ernst, Appl. Phys. Lett. **81**, 2614 (2002).

[15] U. Denker, H. Sigg, and O. G. Schmidt, Materials Science and Engineering B **101**, 89 (2003).

[16] M. De Seta, G. Capellini, F. Evangelisti, and C. Spinella, J. Appl. Phys. **92**, 614 (2002).

[17] M. I. Alonso, M. de la Calle, J. O. Ossó, M. Garriga, and A. R. Goñi, J. Appl. Phys. **98**, 033530 (2005).

[18] V. Magidson, D. V. Regelman, R. Beserman, and K. Dettmer, Appl. Phys. Lett. **73**, 1044 (1998).

[19] D. V. Regelman, V. Magidson, R. Beserman, and K. Dettmer, Thin Solid Films **336**, 73 (1998).

[20] Z. M. Jiang, X. M. Jiang, W. R. Jiang, Q. J. Jia, W. L. Zheng, and D. C. Qian, Appl. Phys. Lett. **76**, 3397 (2000).

[21] X. Z. Liao, J. Zou, D. J. H. Cockayne, Z. M. Jiang, and X. Wang, J. Appl. Phys. **90**, 2725 (2001).

[22] G. Capellini, M. De Seta, and F. Evangelisti, Appl. Phys. Lett. **78**, 303 (2001).

[23] R. Magalhães-Paniago, G. Medeiros-Ribeiro, A. Malachias, S. Kycia, T. I. Kamins, and R. Stan Williams, Phys. Rev. B **66**, 245312 (2002).

[24] M. Floyd, Y. Zhang, K. P. Driver, J. Drucker, P. A. Crozier, and D. J. Smith, Appl. Phys. Lett. **82**, 1473 (2003).

[25] M.-I. Richard, T.-U. Schülli, E. Wintersberger, G. Renaud, and G. Bauer, Thin Solid Films, in press.

[26] U. Denker, M. Stoffel, O. G. Schmidt, and H. Sigg, Appl. Phys Lett, **82**, 454 (2003).

[27] K. Brunner, Rep. Prog. Phys. **65**, 27 (2002).

[28] A. Karim, A. Elfving, M. Larsson, W.-X. Ni, and G. V. Hansson, to be published in Proceedings of the SPIE - The International Society for Optical Engineering, **6129** (2006).

[29] D.B. Williams and C.B. Carter in (1996) *Transmission Electron Microscopy*, p.600, Plenum Press, New York

[30] Q. Xie, A. Madhukar, P. Chen, and N. P. Kobayashi, Phys. Rev. Lett. **75**, 2542 (1995)

[31] T. Mizuno, N. Sugiyama, T. Tezuka, Y. Moriyama, S. Nakaharai, and S. Takagi, Symposium on VLSI, 97 (2003).

[32] T. Mizuno, N. Sugiyama, T. Tezuka, and S. Takagi, IEEE Electron Device Lett. **24**, 266 (2003).

[33] M. Krishnamurthy, Bi-Ke Yang, J. D. Weil, and C. G. Slough, Appl. Phys. Lett. **70**, 49 (1997).

[34] P. Ferrandis, L. Vescan, and B. Holländer, Microelectronics Journal **33**, 541 (2002)

[35] C. G. Van de Walle, and R. M. Martin, Phys. Rev. B **34**, 5621 (1986).

[36] C. W. Liu, J. C. Sturm, Y. R. J. Lacroix, M. L. W. Thewalt, and D. D. Perovic, Appl. Phys. Lett. **65**, 76 (1994).

[37] W.-X. Ni and G. V. Hansson, Phys. Rev B **42**. 3030 (1990).

Chapter 6

Ge dot phototransistors

This section is devoted to the studies of phototransistors based on Ge(dot)/Si low-dimensional heterostructure materials. From the description in chapters 4 and 5, layer design, device layout and detector performance will be treated. The device physics part is mainly collected from refs. 1-3. Most of the results are not reported here and the readers are instead referred to the included papers.

6.1 Heterojunction bipolar phototransistor

A one-dimensional structure of the n-p-n Si/SiGe HBT in the common emitter configuration together with its corresponding band structure are depicted in Fig. 6.1a and b. As shown in the figure, the device consists of two p-n junctions, where the strained p-SiGe region is the base. The Si n-type regions are called emitter and collector, respectively. In normal operation, the device is biased according to the figure. As a result, the emitter-base (e-b) junction is forward biased and the base-collector (b-c) junction is reverse biased. If the base width is smaller than the minority carrier diffusion length, it is possible for electrons to diffuse into the base and further into the collector. Assume that holes are accumulated in the base region via injection from the base contact. A background of positive charges increases the potential and lowers the energy bands in the base, according to the solution of the Poisson's equation. This leads to a decreased energy barrier for the electrons in the emitter to be injected through the base and contribute to the collector current (see Fig. 6.1b). Thus, a small variation of the base current

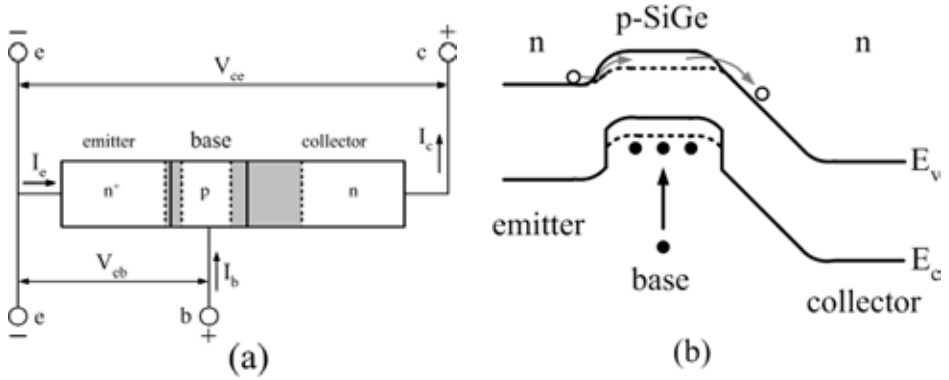

Figure 6.1. The common emitter configuration of a bipolar junction transistor (a). The shaded regions represent the depletion regions. The corresponding energy band diagram of an HBT under operation is illustrated in (b).

can change the collector current by orders of magnitude. The gain in collector current is higher in an HBT than for a conventional BJT, which is shown by

$$\text{BJT:} \quad \beta \equiv \frac{\Delta I_c}{\Delta I_B} \sim \frac{N_{De}}{N_{Ab}} \tag{6.1a}$$

$$\text{HBT:} \quad \beta \equiv \frac{\Delta I_c}{\Delta I_B} \sim \frac{N_{De}}{N_{Ab}} \exp\left(\frac{\Delta E}{k_B T}\right) \tag{6.1b}$$

where ΔI_c and ΔI_b are the changes in collector current and base current, respectively. Moreover, N is the doping concentration and ΔE is the band gap difference between the Si emitter and the strained SiGe base. By analyzing Eqs. 6.1 it turns out that the base width should be small and a high doping level of the emitter compared to the base is required in order to achieve a high current gain. But for an HBT, the current gain is also influenced by the band gap difference, ΔE. The smaller band gap of the SiGe base further decreases the barrier for the emitter electrons and the valence band offset reduces the hole migration from the base to the emitter. This implies that a small increase of the Ge concentration in the base could give an exponential increase of β (mainly because of the increased strain in the material that reduces the band gap). In this case, the requirement for other structural parameters becomes less critical, which makes the device design relatively easy for performance optimization. The speed of the HBT device is another important property. Many requirements to obtain a high

current amplification and a high frequency are however conflicting with each other. The increase in β for an HBT compared to a BJT (due to ΔE) makes it possible to reduce the emitter doping level and still get a high current gain. This reduces the capacitance across the e-b junction, which normally gives a large contribution to the delay time. Decreasing the emitter thickness also reduces the emitter time delay. Another conflicting requirement is the doping level in the base region. A high doping concentration implies a lower base resistance and a high operation frequency of the transistor, but this also decreases the β value. A small base width is however required from the frequency point of view because of the reduced electron transit time through the base. A thin base also increases β, which means that a properly designed HBT normally consists of a narrow base region.

6.1.1 Working principle of the Ge island photo-HBT

The advantage of using an HBT as a detector device (compared to a p-i-n photodiode) is to make use of the gain effect to amplify the generated photocurrent. Consequently, the photo-response will increase compared to a conventional p-i-n photodetector. Fig. 6.2 schematically illustrates the energy band diagram of an HBT Ge-dot phototransistor under operation aimed for light absorption in the wavelength range of 1.3-1.55 μm. The Ge island layers are incorporated in the space-charge region of the b-c junction for absorption, since it is reverse biased during normal operation conditions.

Incident light in the near-infrared range is absorbed via inter-band excitation in the Ge islands, generating electron-hole pairs in the depletion region of the b-c juntion, which are subsequently separated by the applied electric field across the junction. Electrons are swept into the collector while the holes move towards the base region. The holes injected into the base contribute to the base current, which in turn leads to an enhanced electron injection from the emitter through the base into the collector for the same reason as described above. Accordingly, the primary photocurrent is amplified through the transistor, which eventually increases the photo-response of the detector.

Considering the photocurrent gain achieved by this type of HBT device, there is no need of a base contact. The entire base current is supplied by the photo-generated holes moving from the b-c junction into the base. Most of our HBT photodetectors have therefore been fabricated as two-terminal devices, i.e. only emitter and collector metal contacts have been implemented. The drawback with this design is that the device speed is reduced since there is significant hole accumulation with essentially no path for the holes to migrate out of the base.

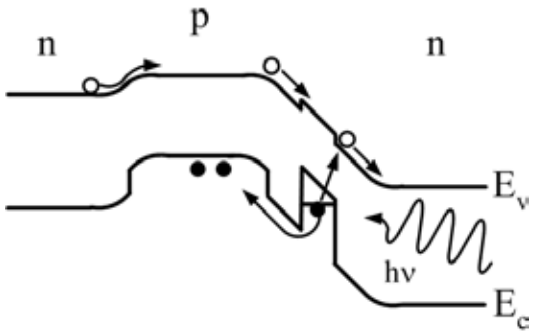

Figure 6.2. Energy band diagram and working principle of a Ge dot HBT phototransistor structure. The island layers are embedded in the b-c junction.

Hence, the hole lifetime in the base region can limit the photocurrent decay time when the device is turned off.

6.1.2 Transistor design

The HBT detectors have been designed as vertical devices, which means that photocurrent transport occurs along the growth direction. The properties of Ge dots, described in chapter 5, influence the performance of a Si/SiGe HBT detector. In order do reach a high photo-response for wavelengths up to at least 1.55 µm, the band gap of the Ge islands should be as low as possible. Therefore, it would be an advantage to produce highly strained Ge islands with a high Ge concentration. High island density will also increase the absorption efficiency. This will also reduce the relative influence of the WL. To fulfill these requirements, the Ge QDs are preferably grown at a relatively low temperature, i.e. around 500 °C. It is still controversial how the dot properties depend on the island shape and this will therefore be excluded from our considerations regarding the design of the phototransistors.

The formation of columns of vertically aligned Ge dots in heterostructures is an interesting and sometimes useful effect for applications. In photodetector applications with vertical carrier transport, however, it has been found that the photo-response is significantly higher from structures containing thick Si spacers with no vertical alignment. This can be explained by the higher probability for the photo-generated holes to be recaptured in the next dot layer during vertical movement in the structure, if the dots are perfectly aligned. In this case, substantial recombination processes will reduce the gain effect and the photocurrent of the phototransistor. In conclusion, the Si spacer layer should therefore be larger than the average island diameter in order to prevent the formation of vertical columns, and hence, recapturing of holes.

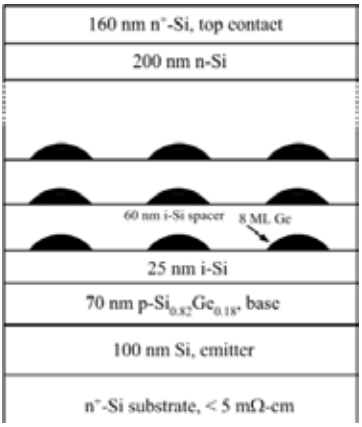

Figure 6.3. Typical layer structure of a Ge dot HBT detector device reported in this work. The vertical alignment is only schematic and is not the case in our structures.

Fig. 6.3 shows a typical layer structure of the heterojunction bipolar phototransistor. The growth started with the emitter (highly n-doped Si) layer from the substrate side, followed by a 70 nm p-SiGe layer containing 18 % Ge with a doping concentration of 1.5×10^{18} cm^{-3}. 5 nm of each side of the base was intrinsic in order to minimize dopant diffusion into the surrounding Si. 10 Ge island layers (8 ML of Ge each) were embedded within the intrinsic region of the b-c junction and separated by 60 nm Si. The collector consisted of a 200 nm lowly doped n-Si layer, followed by an n^+ top layer for ohmic contacts with a reduced series resistance. To demonstrate the effect of current amplification, corresponding p-i-n photodiodes were also grown with 10 Ge dot layers (with the same structural parameters) in the intrinsic region.

A XRD Si(004) θ-2θ scan for the above mentioned HBT detector structure is plotted versus relative angle in Fig. 6.4, together with a simulated diffraction curve. Beside the Si(004) Bragg peak, the high order interference fringes is an evidence of a well-ordered Ge(dot)/Si superlattice. By comparing with simulations, the thickness of the Si spacer and the amount of Ge in each dot layer could be precisely determined (60 nm and 8 ML Ge), which agree well with the design. The broader peak at about 1600 arc seconds below the Si peak is due to diffraction from the SiGe base layer.

Devices were processed as mesas with areas ranging from 0.5×0.5 to 1.5×1.5 mm^2. The sidewalls were passivated by SiO_2, which was deposited by PECVD. Windows were opened in the top collector Al contacts for coupling of normal incident light during photoconductivity measurements. The relatively large device size also allows for measurements using the

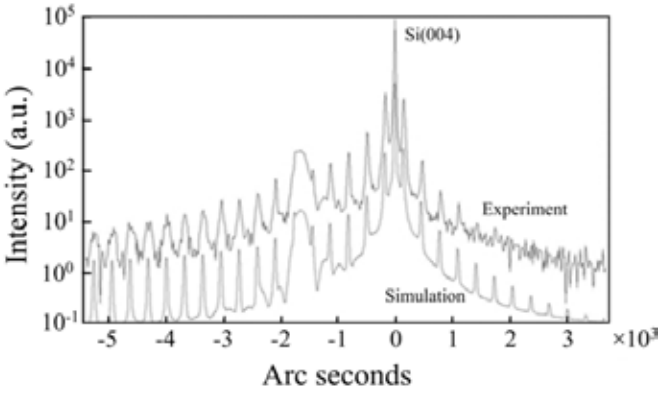

Figure 6.4. XRD θ-2θ scan and a simulated curve for the Ge dot HBT detector. The layer thicknesses and material compositions were in excellent agreement with the design.

waveguide geometry. Representative I-V characteristics, with and without illumination, of the 0.5×0.5 mm^2 HBT detector device are shown in Fig. 6.5. A very low dark current of ~0.01 mA/cm^2 was demonstrated when the b-c junction was reverse biased to V_{bc} = -2 V. Furthermore, the breakdown voltage between the emitter and collector with open base circuit of the HBT, BV_{ceo}, was typically ~ -6 V. Photocurrent modulation by the input optical power could only be observed when the b-c junction was reverse biased. This confirms that the photon absorption only occurs in the Ge islands incorporated in the b-c junction.

6.2 Lateral phototransistor

Lateral Ge dot phototransistors are described in this section. Since the devices involve three terminals for source, drain and gate, respectively, these transistors resemble the FET-type of

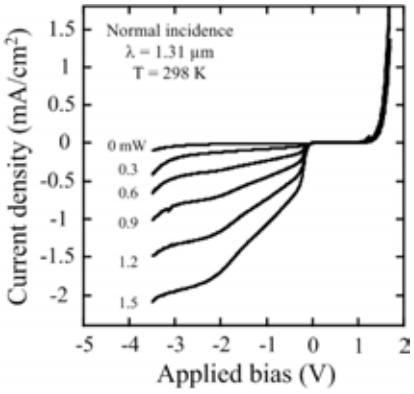

Figure 6.5. Modulation of the photocurrent in the HBT with different power of the incident light.

devices and will therefore sometimes be referred to as FET phototransistors. The working principle is however not the same as for a typical MOSFET device. Consequently, the conventional FET will not be discussed here. This section is thus focused on the layer and device design of the transistors in order to optimize the performance, and the most important purpose of this study was to demonstrate and understand the influence of the gate voltage.

6.2.1 Working principle

The basic working principle of the FET type of Ge dot phototransistors is relatively simple. A number of Ge islands are embedded in intrinsic Si. The near-infrared light absorption occurs in the QDs and the carriers are intended to be separated and contribute to the photocurrent by a lateral applied electric field between the source and drain contacts. Nevertheless, the channel length is very large, partly due to the limitation in pattern line width during photolithography, leading to a comparatively long transit time. The HBT photodetector structure has a total length of about 1 μm, while the lateral detectors have channel lengths of >20 μm. Furthermore, the discreteness of the Ge islands in the in-plane direction makes the carrier transport less efficient in terms of reduced mobility. In addition, transport through the very thin WLs is most likely not favored because of the interface scattering. As a result, the layer structure design and the device layout are more crucial for the FET detectors in order to obtain a high photo-responsivity. The influence of a gate bias is only one parameter that could enhance the photocurrent.

6.2.2 Transistor design

The carrier transport could possibly be more efficient by the implementation of a strained SiGe QW in the neighborhood of a Ge dot layer. The valence band offset allows hole confinement in the QW. Moreover, the enhanced mobility in the strained SiGe layer would also improve the transport properties. Successful Ge-dot/SiGe-QW mid-infrared detectors were previously reported [4]. Since these detectors were operated at low temperatures, the hole transfer from the QDs into the QWs relied on a tunneling process. Thus, a higher photocurrent was observed when the dot-well separation was small. For the near-infrared detectors presented here, the hole transfer can either occur by field emission or thermal emission, since the devices are operated at room temperature. A properly applied gate voltage may control these processes as well as the carrier lifetime by efficient carrier separation.

The position of the SiGe QW could either be below or above a Ge dot layer. There are a few arguments that suggest that it should be located below. From the material aspect there is a

risk that a SiGe layer grown above the dot layer will be undulated, i.e. not completely horizontally flat. This increases the interface scattering probability and reduces the mobility. In addition, the hole migration to the QW could be facilitated by the transfer via the WL energy level if the SiGe QW is below the dot layer.

The SiGe layer thickness and composition are two additional parameters to be considered. The thickness should not be too thin since this can cause interface scattering. Theoretically, a high Ge concentration is desired in the 2-D layer because this increases the strain and hence enhances the mobility and band offset. This layer could also contribute to some extent to the total absorbing medium for the infrared light, particularly at 1.31 μm. However, the formation of islands or lattice relaxation sets the upper limit to the Ge concentration.

For the same reasons as mentioned in section 6.1.2, the islands are preferably grown at low temperatures leading to small sized, high density islands with high Ge concentration. To further minimize the Si-Ge intermixing some structures have been grown at temperatures below 500 °C. Since the main intermixing may occur during island overgrowth, the temperature was ramped down to 370 °C before the initial 10 nm Si capping. Thereafter the temperature was gradually increased during the additional Si capping. In order to avoid dislocations and point defects, the growth rate of Si and Ge was relatively low.

Fig. 6.6a shows a layer design of a lateral Ge-dot/SiGe-QW FET phototransistor. All structures fabricated were based on 10 QD/QW periods grown on an lowly doped p-Si(100) substrate. The SiGe layers were 6 nm and contained around 20% Ge. The intrinsic Si barriers between the QW and QD layers were ranging from 4 to 10 nm in most of the different structures produced. The nominal Ge thickness in the island layers was also varying for the different detector structures. In most cases 6 or 8 ML Ge were deposited. The Si cap layer was totally 60 nm for all structures.

Fig. 6.6b shows a cross-sectional bright-field TEM micrograph of five superlattice periods of one detector device. A distinct and well-reproduced heterostructure is revealed with essentially no correlation between the dot layers because of the large period thickness (~70 nm) compared to the average island diameter (≤ 20 nm). In Fig. 6.6c and d, high-resolution TEM images show the QW/QD layers from the 1st and 10th superlattice periods, respectively. No threading dislocations were observed throughout the entire structure.

The device architecture is of particular importance for the FET detectors. Let us define W as the total length of the source and drain contacts and L as the channel length, i.e. the

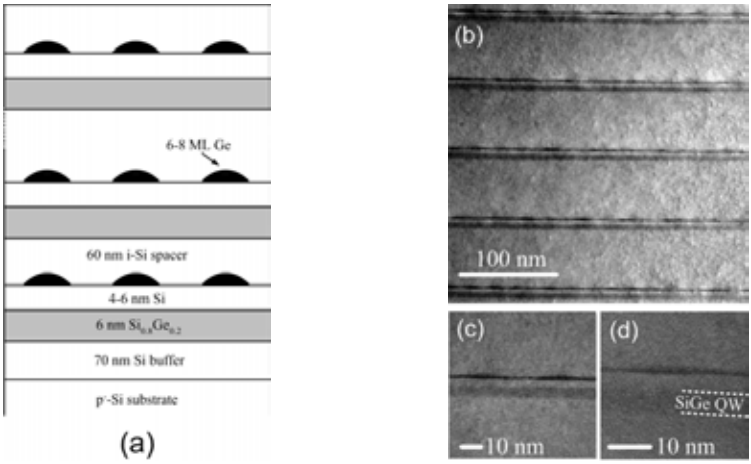

Figure 6.6. Schematic drawing of the lateral Ge dot photodetector layer structure (a), and cross-sectional TEM micrographs of the result after growth (b)-(d).

distance between source and drain electrodes. In principle, a large absorption volume is obtained if *W* is large. Moreover, the channel length is desired to be small for a fast transfer of carriers to the contacts. This will enhance both the photo-responsivity and the device frequency. Thus, for efficient device performance the *W/L* ratio should be high. An alternating multiple comb-finger type of source and drain contacts would fulfill these requirements. In such a design, the distance between them can be rather small while the total length is proportional to the number of fingers. The difference in responsivity at 1.31 μm between detectors processed with $W/L \approx 2$ and $W/L \approx 250$ is shown in Fig. 6.7. The effect is obvious. At high source drain bias, the photo-response seems to be almost proportional to the *W/L* ratio.

Each device was built up by a number of mesas. The comb-finger patterned source and drain electrodes were deposited in such a way that one finger contact overlapped the side edges of two adjacent mesas. The contacts for source and drain were then alternating, as illustrated schematically in Fig. 6.8a. With this design, the active region was properly contacted. After implementation of the source and drain Al electrodes, the samples were normally annealed at ~400 °C for 45 minutes in order to reduce the contact resistance. The gate contact was patterned as a long metal stripe covering all mesas on top. A thick SiO_2 layer was isolating the gate from the substrate. Fig. 6.8b shows a top view optical micrograph of one FET detector.

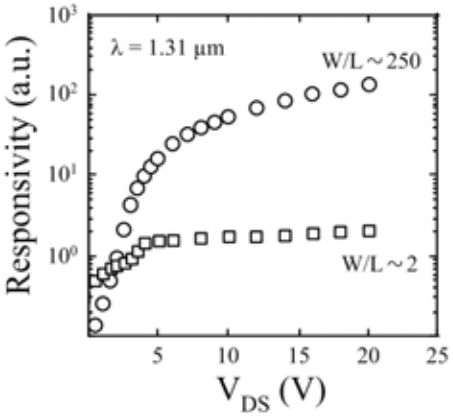

Figure 6.7. The responsivity vs. V_{DS} for two different detector designs. The geometrical factor W/L is one of the important parameters in order to obtain a high photo-responsivity.

Metal-semiconductor FETs (MESFETs) were first fabricated. These phototransistors were processed with a Pt gate contact. The reason for this was to obtain a low gate leakage current since Pt directly deposited on Si forms a high Schottky-barrier contact. Metal-oxide FETs (MOSFETs) were also produced in order to minimize the gate leakage further. As pointed out in section 3.6, the gate oxide was deposited by PECVD. We found that a thickness of ~2000 Å was needed in order to achieve a low enough gate leakage current (≤ 1nA). The PECVD grown oxide was therefore used for both gate isolation (to the substrate) and gate dielectric. Windows were then opened for the source and drain contacts on the sidewalls of the mesas, leaving the top surface capped with oxide for the gate. The thick gate oxide together with a high density of defect charges implied that a high gate voltage was expected to be necessary in order to generate a large enough vertical electric field in the active region.

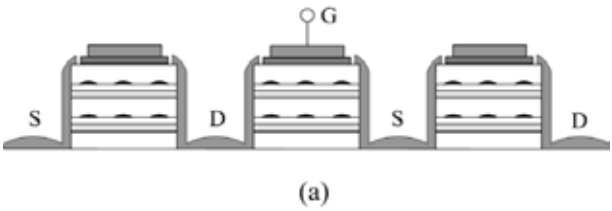

(a)

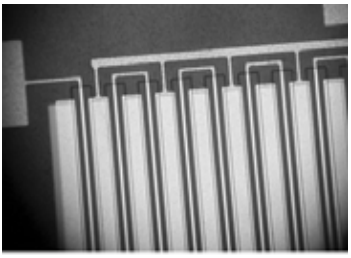

(b)

Figure 6.8. Cross-sectional drawing of a lateral MOS type of photodetector (a), and a top-view taken by an optical microscope (b).

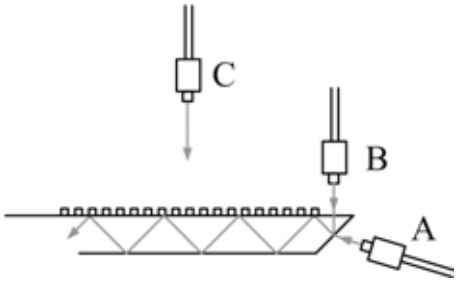

Figure 6.9. Three different photoconductivity measurement setups, denoted A, B and C.

The detector devices were basically processed for waveguide geometry with the light incident from the device edge. One suggestion was to insert the light beam as shown schematically in Fig. 6.9 (setup A). Many samples experienced therefore a polishing procedure before photoconductivity measurements where one edge of the specimen was mechanically polished at an angle of 45° to the surface. Diamond papers were used with grain sizes down to 1 μm to minimize scattering of the incident light. High responsivity could not only be obtained with setup A but also with the more convenient setup B. However, the effect of a polished edge was negligible and many detectors were then processed without polishing and measured using setup A (setup B did not give any photo-response for the unpolished samples). It should also be mentioned that normal incident photoconductivity measurements were performed on some samples via experimental setup C.

References

[1] S. M. Sze, *Semiconductor devices: Physics and Technology*, 2nd edition, published by John Wiley & Sons Inc. 2002.

[2] B. G. Streetman, *Solid State Electronic Devices*, 4th edition, published by Prentice-Hall Inc. 1995.

[3] B. J. Baliga, *Power Semiconductor Devices*, published by PWS Publishing Company,1996.

[4] D. Bougeard, K. Brunner, and G. Abstreiter, Physica E **16**, 609 (2003).

Chapter 7

Summary of included papers

The papers included in the present work are mainly focusing on design, growth and characterization of Ge-dot near-infrared phototransistors. HBT structures with embedded Ge islands in the b-c junction (papers I and II) as well as a Ge-dot/SiGe-QW three terminal FET type detectors (papers III and IV) were processed and studied by means of photoconductivity measurements. In addition, material characterization was employed in order to optimize the device performance (paper V-VII). Si/SiGe nanostructures were investigated by XRD, AFM, TEM, STEM, EDX, PL, etc.

7.1 Paper I

The aim of this work was to develop a Si/SiGe HBT-type phototransistor with several Ge dot layers incorporated in the collector, in order to obtain improved light detectivity at 1.3–1.55 μm. The MBE grown HBT detectors were of n-p-n type and based on a multilayer structure containing 10 Ge-dot layers (8 ML in each layer, separated by 60 nm Si spacer) in the base-collector junction. The transistors were processed for normal incidence or with waveguide geometry where the light was coupled through the transistor edge. The measured breakdown voltage, BV_{ceo}, was about 6 V. Photoconductivity measurements were performed with a tungsten halogen lamp together with a monochromator for selection of wavelength. For the first time, an enhanced photo-response due to the current amplification was demonstrated. Compared to a p-i-n reference photodiode with the same dot layer structure,

photoconductivity measurements showed that the responsivity was improved by a factor of 60 for normal incidence at 1.3 μm. When the light was coupled through the edge of the device, the detectivity was even further enhanced. The photo-responsivity was measured to more than 100 and 5 mA/W at 1.3 and 1.55 μm, respectively. The difficulty to produce a well-defined focused light beam reduced the accuracy of the photo-responsivity values to some extent.

7.1.1 My contributions

Performed the material growth, device processing and characterizations, analyzed the data together with the co-authors, and wrote the manuscript.

7.2 Paper II

This paper was a progress review about the study of the Ge-dot HBT phototransistor. Nanostructure characterization was included as well as new photoconductivity measurement results and time-resolved photo-current experiments. The invention of a novel experimental setup, involving two commercial InGaAs/InP quantum well laser modules as light sources (1.31 and 1.55 μm), provided much higher measurement accuracy for determining the photo-responsivity. The beam was coupled through an optical single mode fiber leading to a better control of the optical power and beam spot size. Furthermore, newly processed HBT transistors showed improved dark current characteristics. A dark current density as low as 0.01 mA/cm^2 at -2 V was demonstrated. By using the above mentioned experimental setup for normal incident light, responsivity values of 50 mA/W at 1.31 μm was directly measured at V_{ce} = -4 V, without involving any rescaling factor due to light coupling. This value was a ~250-fold increase compared to a reference p-i-n diode with the same dot layer structure, due to the current amplification function of the transistor. For a rib waveguide device, a very high responsivity value of about 470 mA/W (V_{ce} = -4V) was obtained at 1.31 μm. Measurements were also performed at 1.55 μm, and the photo-response of the waveguide phototransistor was 25 mAW^{-1}, which was again a large improvement compared with the reference waveguide photodiode (~1 mA/W). Furthermore, spectral photoconductivity results were reported together with a separate analyze of the photo-response during both reverse and forward bias operation using incident light with λ = 850 and 1.31 μm.

7.2.1 My contributions

Performed the material growth and device fabrication, all XRD analyses, electrical characterizations and photoconductivity measurements. Interpreted the data together with the co-authors and wrote the manuscript.

7.3 Paper III

For the first time, a lateral MESFET type of detector processed with three terminals for source, drain and gate was reported. The phototransistor structure was based on Ge-dot/SiGe-QW in Si and intended to absorb light at 1.3-1.55 μm. The 2D SiGe QWs were aimed to facilitate the lateral transport of the photo-carriers more efficient, which was confirmed from photoconductivity measurements on a reference sample without QWs. All detector structures reported in this paper showed high efficiency when near infrared light was incident to the surface normal. With V_G = 0 V, the largest room temperature photo-responsivity value was 140 mA/W and more than 35 mA/W at 1.31 and 1.55 μm, respectively. When the optical power was increased, a sublinear increase of the photo-responsivity proportional to $P_{op}^{0.85}$ was observed, indicating that photo-generated holes were efficiently contributing to the photocurrent. Due to the relatively large gate leakage of the MESFET detectors, this paper did not include the effect of an applied gate voltage.

7.3.1 My contributions

Carried out the growth of the structure and device processing, designed the devices, performed all AFM, XRD and optical characterizations. Analyzed the results with the co-authors and wrote the manuscript.

7.4 Paper IV

In order to reduce the gate leakage, near-infrared MOSFET phototransistors based on a similar heterostructure as in paper III were fabricated and optically characterized by means of photoconductivity and time-resolved photocurrent measurements. The layer structure and device layout was carefully designed to achieve efficient absorption up to λ = 1.55 μm. The superlattice was grown at low temperature by MBE in order to reduce Si-Ge intermixing. The photoresponsivity dependence on the gate bias was demonstrated for the first time. Room temperature measurements with the light coupled through the device edge showed a

significant improvement of the photo-response at negative gate voltage. With V_G above threshold, 350 and >30 mAW^{-1} was measured at 1.31 and 1.55 μm, respectively. This was more than 20 times higher than the response observed at V_G = 0 V. Part of the photocurrent increase was attributed to the longer carrier lifetime. At positive V_G, recombination processes may dominate, resulting in a relatively low photocurrent. The efficient carrier separation at negative V_G increases the photo-response due to the increased carrier lifetime, but reduces the device operation frequency.

7.4.1 My contributions

Performed the material growth, processed the detector devices, and employed all photo-conductivity and time-resolved photocurrent measurements. Drew the major conclusions together with the co-authors, and wrote the paper.

7.5 Paper V

In this paper, recombination processes in MBE grown Ge islands were investigated by photoluminescence. The type II band alignment was observed by observing both spatially indirect and direct transitions. It was also demonstrated that spatially indirect recombinations were dominating at low measurement temperatures while it was a gradual transfer to direct recombinations when the temperature was increased. The dot related luminescence peak of the indirect transition showed an obvious blue shift with excitation power, which was attributed to band bending at the Ge/Si interface.

7.5.1 My contributions

Carried out the growth of the material. Analyzed the data together with the co-authors.

7.6 Paper VI

A more detailed PL study was carried out in this work, where the growth temperature dependence of the two recombination processes was analyzed. The blue shift of the dot related emission peaks with deposition temperature was ascribed to the enhanced Si-Ge alloying during growth. A smaller conduction band offset was suggested for the structures grown at higher temperatures. This was explained by the increased intermixing in the islands, which reduces the strain-induced band offset at the interface. AFM measurements also

revealed a significant increase in dot dimensions with growth temperature, also indicating that the islands were alloyed at higher temperatures.

7.6.1 My contributions

Carried out all the material growth and AFM studies. Discussion and interpretation of the data.

7.7 Paper VII

Strain relaxation and thermal stability of $Si_{0.8}Ge_{0.2}$/Si(110) were studied by means of X-ray reciprocal space mapping. In order to get information about the in-plane lattice mismatch in different crystallographic orientations, mainly (260) and (062) reciprocal lattice points was mapped. SiGe/Si(110) samples containing 20% Ge were exposed to different annealing temperatures up to 1000 °C. The in-plane lattice mismatched was found to be very asymmetric with the major strain relaxation observed in the lateral [001] direction. This was associated to the formation and propagation of $a/2\langle 110 \rangle$ total dislocations with Burgers vectors lying within the {111} glide planes. The Ge concentration of arbitrarily relaxed SiGe(110) layers could be accurately determined from the bulk elastic theory for a homogeneous deformation.

7.7.1 My contributions

Carried out the material deposition and the XRD reciprocal space mapping together with the second author. Drew the conclusions together with the co-authors, and wrote the manuscript.